

Spring 2023

Nondestructive Damage Detection and Stress Corrosion Crack Mitigation in Stainless Steel Plates

Andrew Philip Campbell

Follow this and additional works at: <https://scholarcommons.sc.edu/etd>



Part of the [Mechanical Engineering Commons](#)

Recommended Citation

Campbell, A. P.(2023). *Nondestructive Damage Detection and Stress Corrosion Crack Mitigation in Stainless Steel Plates*. (Master's thesis). Retrieved from <https://scholarcommons.sc.edu/etd/7284>

This Open Access Thesis is brought to you by Scholar Commons. It has been accepted for inclusion in Theses and Dissertations by an authorized administrator of Scholar Commons. For more information, please contact digres@mailbox.sc.edu.

Nondestructive Damage Detection and Stress Corrosion Crack Mitigation in Stainless
Steel Plates

By

Andrew Philip Campbell

Bachelor of Science

University of South Carolina, 2020

Submitted in Partial Fulfillment of the Requirements

For the Degree of Master of Science in

Mechanical Engineering

College of Engineering and Computing

University of South Carolina

2022

Accepted by:

Lingyu Yu, Director of Thesis

Yuh J. Chao, Second Reader

Cheryl L. Addy, Interim Vice Provost, and Dean of the Graduate School

© Copyright by Andrew Philip Campbell, 2023
All Rights Reserved.

ACKNOWLEDGMENTS

I would like to thank my advisor Dr. Lingyu Yu for her continued support and guidance. Thank you to the Visualized Structural Health Monitoring (VSHM) for all their help and support. Thank you to all our collaborators, Dr. Poh-Sang Lam, Dr. Andy Duncan, Dr. Bob Sindelar from Savannah River National Laboratory (SRNL), and Dr. Kallie Metzger, Jorie Walters at Westinghouse, and Dr. Victor Giurgiutiu and Dr. Hanfei Mei from the University of South Carolina. Thank you to my family and friends for their support.

The research work in this thesis was supported by the University of South Carolina, SC NASA EPSCoR 2021/2022 Research Grant Program, and the U.S. Department of Energy's Nuclear Engineering University Program (NEUP) under grant numbers DE-NE0008959 and DE-NE0008894.

ABSTRACT

The ability to inspect and detect damage within a structure without permanent damage has broad appeal in a range of engineering applications from aerospace structures to nuclear facilities. Non-destructive evaluation (NDE) using guided ultrasonic Lamb waves has growing potential and popularity in these fields. Lamb waves are known for being sensitive to material properties and various defects across the thickness such as cracks in metallic structures and delamination or debonding in composite structures. Research has also been done on the development of fully non-contact system that generates and detects Lamb waves, particularly focused on the use of pulsed laser for generation and laser doppler vibrometer for sensing. In the past, the NDE system has been set up for situations where access to both sides of the sample is available. This creates the limitation where situations where access to only one side is permitted cannot be accurately re-created. Another limitation lies in the majority of sensing with laser doppler vibrometer being achieved through velocity measurement. In addition, research of NDE is often focused on the detection and evaluation of the damage leaving the mitigation of the damage less discussed, if identified. Therefore, this thesis is aimed at addressing these subjects.

In part I this thesis explores the upgrading and development of a laboratory testing configuration that accommodates a variety of fully non-contacting Lamb wave NDE system consisting of a pulsed laser and a scanning laser doppler vibrometer. The original system was re-designed and re-configured to accommodate both same-side (with

both pulsed laser and scanning laser doppler vibrometer access to the same surface of the test plate) and opposite-side inspection through optical re-directing of laser from pulsed laser. Special considerations are given to high energy invisible laser from the pulsed laser being used in this study. The system has been tested with a range of samples constructed of simple or complex geometries, including thin foils and small diameter tubing. The results show that Lamb waves can be actuated and detected at frequencies up to 4 MHz.

In part II this thesis explores a potential solution to stress corrosion cracking by use of an engineered carbon fiber reinforced polymer patch. Patch design, material selection, and a detailed installation procedure are explored and developed in this study. To evaluate the patch integrity as well as the crack mitigation with the patch, a set of tests have been designed. We first performed effectiveness testing to verify the load bearing ability of the patch. After that, an environmental chamber that can accommodate temperature (room to 50°C), humidity, and marine environment (salt water corrosivity) was designed and selected samples were placed for an extended period for exposure. We have evaluated and shown that the proposed patch can increase the load bearing ability of the stainless-steel substrate. Secondly, we have successfully developed a controlled environment for evaluating the durability of the patch when exposed to a variety of environmental conditions including temperatures reaching 50°C and humidity reaching 85%.

In summary, this thesis work explores a fully non-contact Lamb wave NDE System that can provide same-side or opposite-side inspection for a variety of structures

with varying geometries. A composite patch repairing methodology is also explored to mitigate the structural integrity if cracking occurs. We showed that the patch has satisfactory integrity with clear load bearing increase for patched samples of up to 500 lbf and can prevent the crack growth. In the future, further exploration can be done by investigation into expanding the frequency limits of the SLDV sensing system, performing studies into the detection of and integrity verification of coatings applied to thin foils and tubes, and review possibilities on expanding the durability of the bonded CFRP patches.

TABLE OF CONTENTS

ACKNOWLEDGMENTS	iii
ABSTRACT	iv
TABLE OF CONTENTS	vii
LIST OF TABLES	ix
LIST OF FIGURES	x
LIST OF GRAPHS	xiv
LIST OF SYMBOLS.....	xv
LIST OF ABBREVIATIONS	xvi
CHAPTER 1 PART I CRACK DETECTION BY NON-CONTACTING ULTRASONIC INSPECTION	
METHODS	1
CHAPTER 2 PL-SLDV FULLY NON-CONTACT NDE SYSTEM CONFIGURATION.....	3
CHAPTER 3 ULTRASONIC SENSING WITH DISPLACMENT MEASUREMENT.....	14
CHAPTER 4 LAMB WAVE DETECTION ON COMPLEX STRUCTURES	18
CHAPTER 5 PART I CONCLUSION.....	24
CHAPTER 6 PART II CRACK MITIGATION USING ENGINEERED COMPOSITE PATCH.....	25
CHAPTER 7 PATCH DESIGN AND INSTALLATION.....	28

CHAPTER 8 PATCH STRENGTH AND REPAIRING EVALUATION.....	36
CHAPTER 9 PATCH DURABILITY STUDY IN NEAR MARINE ENVIRONMENTS	51
CHAPTER 10 PART II CONCLUSION	61
REFERENCES	62

LIST OF TABLES

Table 2.1 Available decoders for Polytec PSV-300-M2 SLDV from user's manual.....	5
Table 8.1 Tested samples and their resulting max stresses.....	41
Table 8.2 Redesigned test samples and stress concentration results.	43
Table 9.1 Preliminary accelerated corrosive environment exposure test groups.....	55
Table 9.2 Table 7.2: Exposure testing environmental conditions by round.	57

LIST OF FIGURES

Figure 2.1 A) Automatic mode timing for flashlamp and Q-switch signals B) plano-convex focusing lens diagram.....	4
Figure 2.2 A) Diagram of opposite side testing configuration B) Laboratory configurations for opposite.	5
Figure 2.3 Diagram of experimental setup using the PL-SLDV system A) current layout: opposite side testing B) proposed layout: same side testing.....	6
Figure 2.4 Proposed system configurations for same side PL-SLDV testing A) Design #1 B) Design #2.	8
Figure 2.5 Mirror components for redirecting PL for same side testing A) Mirror with silver protective coating B) Kinematic stand C) Stand arm.	9
Figure 2.6 : Experimental arrangements of PL-SLDV system A) Same-side testing B) Opposite-side testing.....	10
Figure 2.7 Actuation and sensing schematic for verification testing of new laboratory configurations.	11
Figure 2.8 Sensing results for verification tests of 1mm aluminum. time-space wavefields A) opposite side sensing, and C) same side; fk spectrum of B) opposite side sensing, and D) same side sensing. Highlights of shockwave.....	12
Figure 2.9 Sensing results for verification tests of 1mm aluminum. time-space wavefields A) Original configuration, and C) New configuration; fk spectrum of B) Original configuration and D) New configuration.....	13

Figure 3.1 PZT-SLDV DD-300 Testing configuration, A) Fundamental diagram B) Experimental setup C) Actuation and sensing schematic. 15

Figure 3.2 Sensing results for 240 kHz and 360 kHz PZT-SLDV tests Velocity vs. Displacement decoders. Normalized fk spectrum comparison A) 240 kHz with VD-07 20 B) 240 kHz with DD-300 C) 360 kHz with VD-09 20 D) 360 kHz with DD-300. 16

Figure 3.3 Sensing results for 120 kHz PZT-SLDV tests Velocity vs. Displacement decoders. time-space A) wavefield from VD-07 B) Normalized fk spectrum from VD-09 C) wavefield from DD-300 D) Normalized fk spectrum from DD-300... 16

Figure 3.4 Sensing results for PZT-SLDV tests Velocity vs. Displacement decoders waveform comparison A) 120kHz VD-07 20 vs DD-300 B) 240kHz VD-07 20 vs DD-300 C) 360kHz VD-09 20 vs DD-300. 17

Figure 4.1 Same sided PL-SLDV testing arrangement for tubular samples A) Custom grips, B) Actuation and sensing schematic. 19

Figure 4.2 Sensing results for AL tube sample tested at 30 mJ PL-SLDV tests Velocity vs. Displacement decoders. A) VD-09 20 wavefield B) VD-09 20 fk Spectrum C) DD-300 wavefield D) DD-300 fk Spectrum..... 20

Figure 4.3 Sensing results for SS tube sample tested at 30 mJ PL-SLDV tests Velocity vs. Displacement decoders. A) VD-09 20 wavefield B) VD-09 20 fk Spectrum C) DD-300 wavefield D) DD-300 fk Spectrum..... 21

Figure 4.4 Thin foil PL-SLDV testing A) gripping solution. B) Actuation and sensing schematic..... 22

Figure 4.5 76 μm Al foil sample tested at 30 mJ A) VD-09 200 wavefield B) VD-09 200
fk Spectrum C) DD-300 wavefield D) DD-300 fk Spectrum E) DD-300 fk
Spectrum from 1500 to 3000 kHz decreased colormap..... 22

Figure 4.6 25.4 μm Al foil sample tested at 30 mJ A) VD-09 200 wavefield B) VD-09
200 fk Spectrum C) DD-300 wavefield D) DD-300 fk Spectrum E) DD-300 fk
Spectrum from 1500 to 3000 kHz decreased colormap..... 23

Figure 7.1 Patch types after bonding, A) Rock West Prepreg, B) Fibre Glast plain
unidirectional type 1, C) Fibre Glast plain unidirectional type 2, D) Control, E)
Preliminary test samples 1- 6 going from left to right..... 31

Figure 7.2 A) 3D printed Proof-of-concept prototype adhesive mold. B) Illustration of
adhesive application pattern. A 75 mm by 50 mm CFRP composite. 33

Figure 7.3 Preliminary test sample geometry. A) 3 mm hole B) 10 mm slot..... 34

Figure 8.1 Selected testing equipment A) MTS 810 Material Testing System B) MTX
458.20 Microcontroller. 37

Figure 8.2 A) 3D model of original grip design sent to machine shop. B) evidence of
slippage C) Final Grip..... 38

Figure 8.3 Examples of sample designs used in stress concentration study with
descriptions. 39

Figure 8.4 A) Example of simulation loading B) Example of stress concentration
colormap of sample V1..... 40

Figure 8.5 Stress concentration study results A) Sample V20 B) Final selected crack
starter geometry. 42

Figure 8.6 Tools used for crack starter cutting A) Dremel model 4300 76-piece variable speed corded multipurpose rotary tool with hard case purchased from Lowes.[28] (B, top and bottom) Sample cutting jig made of Blue PLA..... 45

Figure 8.7 A) Control test sample #1 before and after testing B) Patched test sample #1 before and after testing C) Close up on deformation seen on baseline test 3 and Patch Test 1..... 46

Figure 8.8 A) Final tension testing sample design B) Final test sample loaded for testing C) Final Patched test sample..... 47

Figure 9.1 Design graphic for environmental chamber. 53

Figure 9.2 Proof of concept construction of environmental chamber 53

Figure 9.3 Environmental chamber with refinements implemented and labeled, NOT shown is drain. 54

Figure 9.4 Sample arrangement inside the environmental chamber. 55

Figure 9.5 Example test samples: A) Control no exposure B) 15 days exposed patched C) 30 days exposed unpatched D) 30 days exposed patched..... 56

LIST OF GRAPHS

Graph 8.2 Group 1 Results.....	47
Graph 8.1 Control Results.....	47
Graph 8.3 Round 1 Unpatched samples only.....	48
Graph 8.4 Round 2 sample 1 Patched VS. Unpatched	49
Graph 8.5 Round 2 sample 2 Patched VS. Unpatched	49
Graph 8.6 Round 2 sample 3 Patched VS. Unpatched	49
Graph 8.7 Round 4 Patched VS. Unpatched.....	50
Graph 8.8 Round 3 Patched VS. Unpatched.....	50
Graph 9.1 Preliminary Patches sample comparison between Groups 0 and 1.....	57
Graph 9.2 Comparison of Round 2 plate one groups.....	58
Graph 9.3 Comparison of Round 2 plate two groups	58
Graph 9.4 Round 3 pathed sample comparison	59
Graph 9.5 Round 4 Patched Samples.....	60
Graph 9.6 Round 4 Control Samples	60

LIST OF SYMBOLS

fk Frequency-wavenumber in relation to the Lamb wave dispersion curves

GPa Gigapascal

kHz Unit of frequency, kilohertz

MHz Unit of frequency, Megahertz

mJ Unit of energy, millijoule

” Inches

° Degrees

LIST OF ABBREVIATIONS

CFRP.....	Carbon Fiber Reinforced Polymer
CISCC.....	Chloride-Induced Stress Corrosion Cracking
EDM.....	Electrical Discharge Machining
FRP.....	Fiber Reinforced Polymer
GFRP.....	Glass Fiber Reinforced Polymer
HAZ.....	Heat Affected Zone
NDE.....	Nondestructive Evaluation
PL.....	Pulsed Laser
PZT.....	Piezoelectric Transducer
SCC.....	Stress Corrosion Crack
SLDV.....	Scanning Laser Doppler Vibrometer
SR.....	Stiffness Ratio
SS.....	Stainless Steel

CHAPTER 1 PART I
CRACK DETECTION BY NON-CONTACTING ULTRASONIC
INSPECTION METHODS

The use of guided ultrasonic waves for nondestructive evaluation (NDE) has been well studied by previous works present in literature [1-5]. These guided waves are often referred to as Lamb waves when they propagate in plate like structures. Lamb wave based NDE has been shown to be an effective method for material evaluation and damage detection [1-5]. The Lamb waves have been shown excited or sensed by a variety of actuators and sensors. The fully non-contact NDE systems refer to those who adopt actuators and sensors that are not physically in touch with the structures, presenting minimum intrusion to the structures being inspected. Pulsed laser (PL) actuation through thermos-elastic effects for actuation and scanning laser doppler vibrometer (SLDV) through doppler effect for wave motion sensing have been developed as seen in [1-5]. Many often the wave motion sensing through SLDV is achieved by velocity measurements. When performing the actuation and sensing, traditionally for the detection of damage such as cracks in metallic structures or debonding between laminated composite layers Lamb waves with frequencies below 1 MHz.mm are used. For many structures that are thicker than 1 mm, which means the frequencies involved are less than 1 MHz. If the method is used in structures that are significantly thinner than 1 mm, higher frequencies above 1 MHz are needed.

The objectives in Part 1 of this thesis are:

- A) Configure and develop testing arrangements for a fully non-contacting guided wave PL-SLDV NDE system for laboratory testing, with an emphasis on the ability to inspect with access to a single side and both sides of the test specimen.
- B) Explore and establish an alternative wave motion sensing through displacement measurement with the SLDV compared to the existing velocity measurement.
- C) Perform high frequency and wideband guided wave sensing on structures, focusing on exploring frequencies above 1 MHz and the continued verification of the displacement measurement configuration.

CHAPTER 2

PL-SLDV FULLY NON-CONTACT NDE SYSTEM CONFIGURATION

In our laboratory a Quantel CFR 400 Q-switch PL is used as a method to generate Lamb waves. This model can produce energy up to 332 mJ which is controlled from 0% to 100% with a built-in attenuator. The PL produces emits a beam with a diameter of 8 mm at a wavelength of 1064 nm. The PL width of excitation is 7 ns measured full width at half maximum. There is a 70 ns delay after the Q-Switch trigger pulse. The diagram in Figure 2.1A illustrates the Q-switching for laser pulse generation from the Quantel manual.

When the laser pulse contacts the surface, the exciting surface area is heated rapidly to create a sudden thermal expansion [2]. Due to the small size of this heated area, there is a limit to how much expansion can be created. When the excitation surface area reaches the boiling point of the material, nanometers of the expanding material will evaporate, and the recoil effect generates the ultrasonic waves [2]. The laser energy can be focused into a smaller area to create higher intensity through the use of optical focusing lens. Figure 2.1B diagram illustrates a plano-convex line focusing lens that is used in conjunction with the PL. This lens is used to direct the laser into an intense line excitation area, rather than the circular area normally produced. This new excitation area creates a straight crested Lamb wave in place of the circular Lamb wave [2]. More details

of pulsed laser for ultrasonic generation can be found in [7] This thesis study will be only focused on the adoption for wave generation.

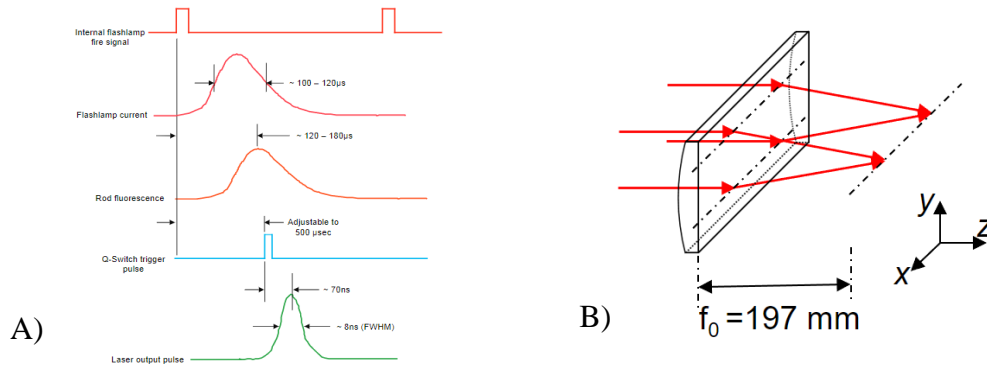


Figure 2.1 A) Automatic mode timing for flashlamp and Q-switch signals B) plano-convex focusing lens diagram.

The Polytec PSV-400-M2 scanning laser doppler vibrometer model is employed for multidimensional time-space wavefield sensing. This system scans a predefined line or area by “directing the laser beam to multiple points through two mirrors inside the laser head driven by galvanometric actuators” [2]. This system uses the doppler frequency-shift effect on the laser beam to measure the surface particle motion. This measurement is taken at each point in the predefined path and is used to detect propagating Lamb waves. The data acquisition system used by the SLDV has several aspects that can be controlled, the number of averages per measurement point, sampling frequency, spatial resolution, and decoder selection. Each decoder has a maximum sensing range that it can be used for, this system has offerings that range from 20 kHz to 20 MHz. The decoders used in this study with their ranges are given below in Table 2.1

Table 2.1 Available decoders for Polytec PSV-300-M2 SLDV from user's manual

Velocity Decoders	$\frac{mm}{s} / v$	Maximum Sensing Range
VD-07	10, 20, 50	350 kHz
VD-09	20	1.2 MHz
VD-09	50, 100	1.5 MHz
VD-09	200	2.5 MHz
Displacement Decoders	$\frac{mm}{s} / v$	Maximum Sensing Range
DD-300	50	20 MHz

When using both the PL and the SLDV systems it is important that the angle that the lasers approach the plate remains as close to 90° as possible. This allows for maximum energy transfer from the PL, and the most accurate reading from the SLDV system. The PL-SLDV system was originally configured and set up for PL and SLDV to assess both sides of the test sample, one for the pulse laser and the other for the SLDV in consideration of the size of the components (seen in Figure 2.2B) and the safety requirements of the PL. This is referred to as opposite side testing and illustrated in Figure 2.2A

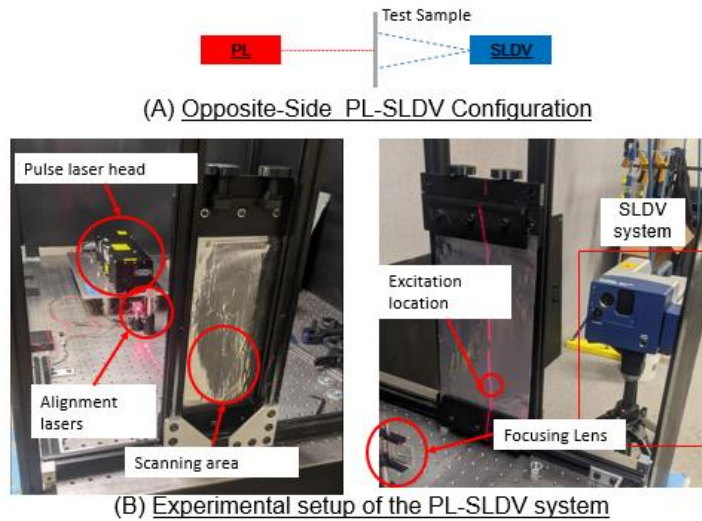


Figure 2.2 A) Diagram of opposite side testing configuration B) Laboratory configurations for opposite.

This form of opposite-side testing has its benefits and its limitations. The benefit is that the PL can be maneuvered and used to impact the sample at any location without effecting the SLDV system, and the same is true for the SLDV being placed anywhere, closer or farther away from the samples as needed, without considerations for possible interfering with the PL path. However, the opposite side testing has its limitations in two main forms. First, sample thickness, the Lamb waves that are used for damage detection create a limitation on the thickness because they cannot propagate through thick samples reliably. The second limitation is application access to both sides of the sample on site is not always available or is impractical. For these reasons, a new configuration is needed so that the same side of the test sample is used. Figure 2.3 shows the system layouts for A) opposite side and B) a same side configuration.

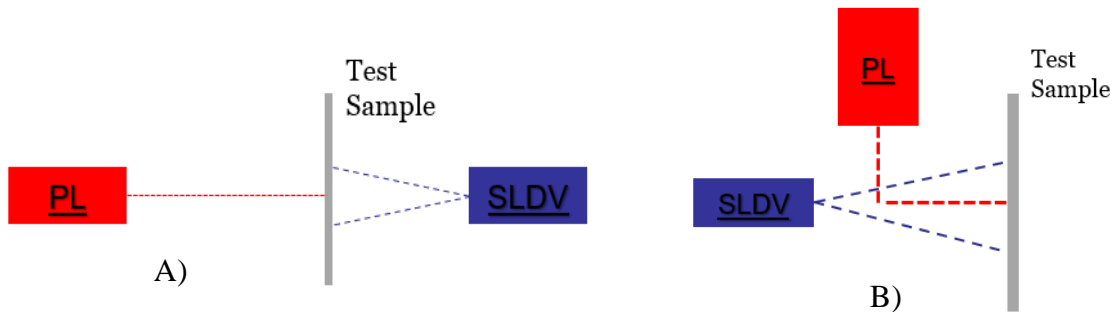


Figure 2.3 Diagram of experimental setup using the PL-SLDV system A) current layout: opposite side testing B) proposed layout: same side testing.

2.1 PL-SLDV SYSTEM SETUP WITH LASER SAFETY

The Objective was to design and construct a PL-SLDV system configurations that would allow for testing to be done that only needed access to one side of the test sample, referred to as same side testing. To do this we needed to completely redesign the current configuration. The major design requirements were 1) the antivibration table should not be moved, 2) the current level of safety must be maintained, and 3) the system must be

able to facilitate both same side and opposite side testing. The secondary requirements are imposed by the SLDV and pulse laser systems that are in use by the laboratory. The SLDV must be mounted so that it is normal to the sample surface with a clear line of sight to the sample, at a distance that is adjustable from 500 mm to 700 mm away. The pulse laser requires that it impacts the sample at an angle of no more than 20° from normal, and that there must be room allotted for focusing lenses, 300 mm along the path of the laser. Major requirement #2 can be achieved first by maintaining that there are no gaps or points in the laser enclosure that would allow for the laser or its reflection to escape and using the same thickness aluminum with the same non-reflective surface finish.

Two original designs were created, design one and design two both shown below, (Figure 2.4). Design one has a tight-fitting cover that follows the path of the laser as it is reflected 90° off a mirror. The SLDV would be placed above these covers, while the test sample is placed in a stand that positions the sample off the edges of the table so that it can be adjusted up and down to change the pulse laser's impact location. This design offers the benefits of needing little new material, and the pulse laser did not need to be moved. The cons of this design include a reduced SLDV scanning area because of the shielding, and little way to change the distance from the SLDV to the test sample. Design two has a large shielding box that encloses the whole tabletop, where the test sample is held by a test stand mounted to the top of the table, and a mirror would again be used to redirect the pulse laser beam 90° . In this design an access hole is needed for the SLDV to be inserted into the box. This design offers the benefits of increased SLDV scanning area, simple adjustability for a variety of spatial resolutions, and simple changes can be made

for using same side or opposite side testing. The cons of this design is that all new shielding panels are needed and several other new parts, and the pulse laser should be moved for maximum adjustability.

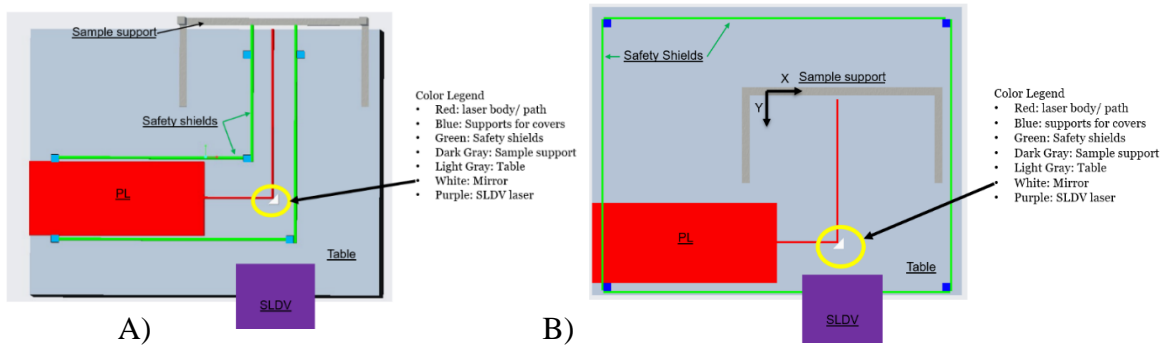


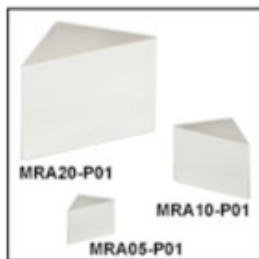
Figure 2.4 Proposed system configurations for same side PL-SLDV testing A) Design #1 B) Design #2.

The final design follows that of the second design, with minor additions and changes. That includes a defined 36-inch box height, the pulse laser is not moved. This was chosen because it met all the major design requirements, while being able to be reconfigured in the most ways. This design allows for same side testing at a variety of spatial resolutions, and with minor changes can allow for the same variety in opposite side testing.

The University of South Carolina has a published radiation safety manual that outlines the key safety requirements for Laser operation [8], as a part of these requirements all users must have completed the university approved laser safety course, and that for a class 4 laser there can be no path for the beam or a reflection of the beam to escape. To maintain adherence to this standard of lab safety, panels of .08” thick 3003-H14 aluminum sheets were used for the external panels and attached to T-Slotted aluminum frame structure for the shielding box. Panel hangers are used on the side of the table as this is the access point of this design, this side will be removed to add the

samples, or adjust the testing arrangement. handles were added to the access panel to make it easier to maneuver into place. The joints in the panels are arranged so that there are limited points of possible leakage, or laser energy escaping. When selecting the correct mirror for use with our pulse laser Thorlabs's was used and three potential options were found, a protected aluminum, a protected silver, and a protected gold. All these coatings offered reflectance of greater than 90% for a range that included our 1064 nm laser. The protected silver was selected because it offered the highest reflectivity at 97.5 % and the highest damage threshold of 3 J/cm² at 1064nm, 10ns, 10 Hz, 1.000 mm. A kinematic prism mount and an adjustable prism clamp were also purchased to insure proper mounting and compatibility with the existing hardware in the lab.

Protected Silver



A)



B)



C)

Figure 2.5 Mirror components for redirecting PL for same side testing A) Mirror with silver protective coating B) Kinematic stand C) Stand arm.

The sample stand was constructed using more T-Slotted aluminum, and associated brackets. This construction method allows for easy adjustability to accommodate the range of samples that the team has. The test stand was then bolted to the table using 2 bolts. The mirror is placed to intersect the existing laser path, such that it will redirect the beam 90° to impact a test sample mounted in the stand. With the mirror stand in place the laser alignment procedure was created to achieve an accurate and repeatable laser path. With the laser alignment complete, the system was ready to conduct same side tests for comparison with previous opposite side test for verification of system. To reestablish the opposite side testing capabilities, replacement panels were created so that the opening for the SLDV system is sealed, there is an opening directly opposite the PL to allow sensing on the back of a test sample.

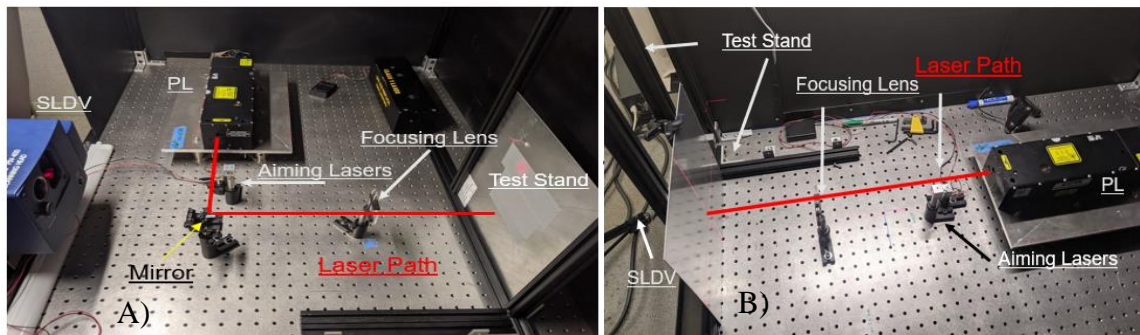


Figure 2.6 : Experimental arrangements of PL-SLDV system A) Same-side testing B) Opposite-side testing

2.2 SAME SIDE SLDV SENSING SETUP

To verify that the new system configurations have had no negative effects on our testing results a series of tests were conducted using a 1 mm aluminum plate, and the line focusing lens. The standard for comparison of these tests was taken before any system changes were made. The first comparison made to show that the same side system is

operational. Then a comparison between opposite sides before any changes were made, and then after all the changes, this is to show that the integrity of the system has not been compromised. The actuation and sensing schematic are shown in Figure 2.7, with a line scan 10 to 80 mm along y direction from the PL source. The PL excitation energy is set as 10 mJ (3% of the full energy). The SLDV sampling rate is 25.6 MHz and the average is set as 10.

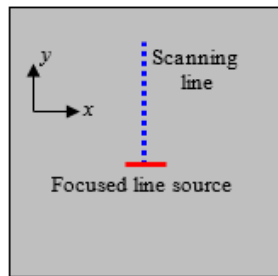


Figure 2.7 Actuation and sensing schematic for verification testing of new laboratory configurations.

The resulting time-space wavefields measured on the opposite side before changes, and the same side are plotted in Figure 2.8A and 2.8C respectively. The time-space wavefields show that a strong A0 is excited in both, however a large slow-moving wave appears in the same side test. Through 2D Fourier transform, the frequency-wavenumber (fk) spectrum is obtained and presented in Figure 2.8B and 2.8D for the opposite side and same side respectively. The figures show that the excited fk spectrum

match the theoretical A0 dispersion curve. The fk spectrum for the same side shows the additional wave strongly with a frequency below 200 kHz.

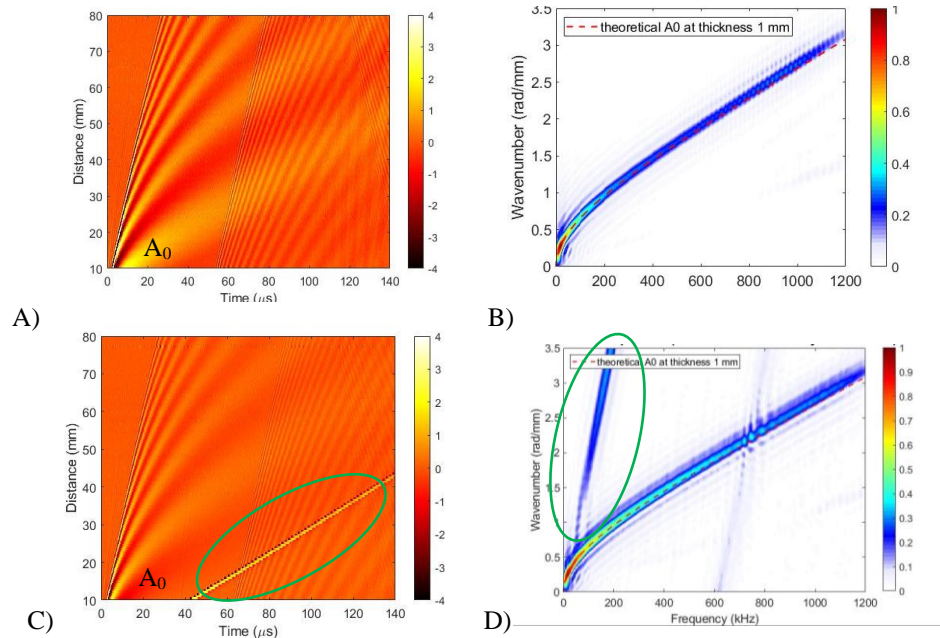


Figure 2.8 Sensing results for verification tests of 1mm aluminum. time-space wavefields A) opposite side sensing, and C) same side; fk spectrum of B) opposite side sensing, and D) same side sensing. Highlights of shockwave.

From these results we can see that there is an inversion in the colormap due to the change in relative motion direction as was expected. The appearance of the strong low frequency slow moving shockwave seen in the same side tests was not expected, however it appears to have a limited effect on the ability to perform damage detection due to its propagation speed.

The resulted time-space wavefields measured on the opposite side before any changes, and in the opposite side configuration after are plotted in Figure 2.9A and 2.9C respectively. The time-space wavefields show that a strong A0 is exciting in both. Through 2D Fourier transform, the frequency-wavenumber (fk) spectrum are obtained

and presented in Figure 2.9B and 2.9D for the before and after respectively. Both figures show that the excited fk spectrum agree well with the theoretical A_0 dispersion curve.

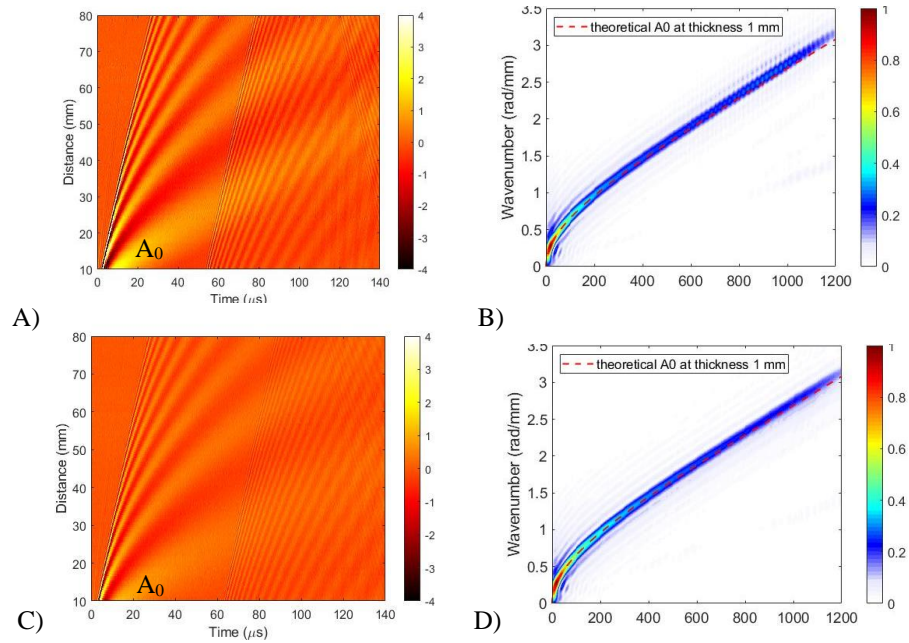


Figure 2.9 Sensing results for verification tests of 1mm aluminum. time-space wavefields A) Original configuration, and C) New configuration; fk spectrum of B) Original configuration and D) New configuration.

CHAPTER 3

ULTRASONIC SENSING WITH DISPLACEMENT MEASUREMENT

As discussed previously, the PSV-400 SLDV system offers multiple sensing decoders, with the most used being the velocity decoders such as VD-07 and VD-09. However, these velocity decoders have a limitation on the maximum nominal frequency of 2.5 MHz. On the contrary the displacement decoders can measure much higher frequencies. The available displacement decoder for PSV-400 is DD-300 with a designed upper frequency range of 20 MHz. This chapter focuses on developing the ultrasonic guided waves sensing ability of DD-300 as an alternative inspection technique to velocity measurement, as well as explore its limit for high frequency testing. To provide reliable Lamb waves frequency information a traditional piezoelectric transducer (PZT) is bonded to the test sample as an actuator to create Lamb waves at test excitation frequency. The PZT-SLDV system has been previously established in the lab [2] and is shown below in Figure 3.1.

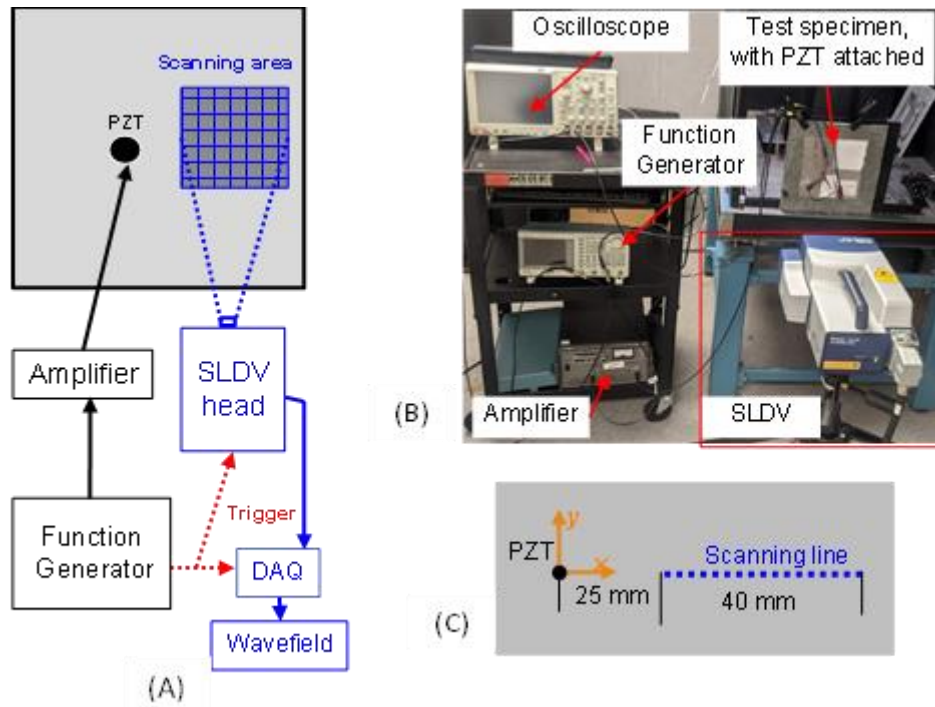


Figure 3.1 PZT-SLDV DD-300 Testing configuration, A) Fundamental diagram B) Experimental setup C) Actuation and sensing schematic.

To investigate the decoder selection a sample of 1 mm thick, 2024-T3 aluminum plate was used. The actuation signal sent to the PZT was a 3-count tone burst with a burst rate of 1 ms. The SLDV was set to scan over a 40 mm line that was 25 mm away from the PZT (Figure 3.3C). Multiple tests at frequencies ranging from 120 kHz to 360 kHz were used to establish a baseline understanding of the decoders. The SLDV system used in our lab can record data simultaneously on 2 channels (VOL, and Ref 1), with the VOL channel for the velocity decoder and Ref 1 for the displacement decoder. The decoders were compared in terms of recording the proper information regarding Lamb wave propagation, through the evaluations of the directly recorded wavefield, the waveforms, and the fk spectrum analysis of the wavefields.

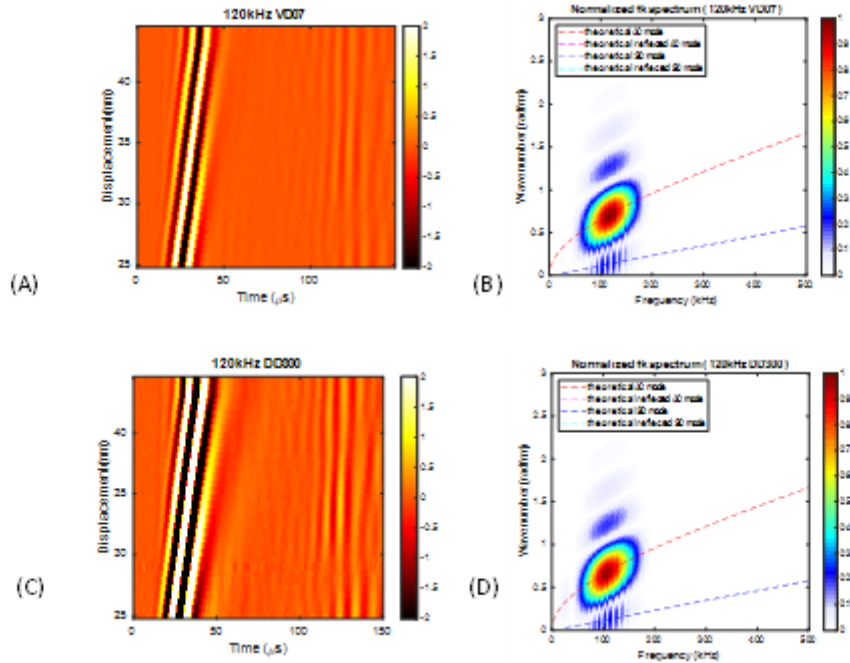


Figure 3.3 Sensing results for 120 kHz PZT-SLDV tests Velocity vs. Displacement decoders. time-space A) wavefield from VD-07 B) Normalized fk spectrum from VD-09 C) wavefield from DD-300 D) Normalized fk spectrum from DD-300.

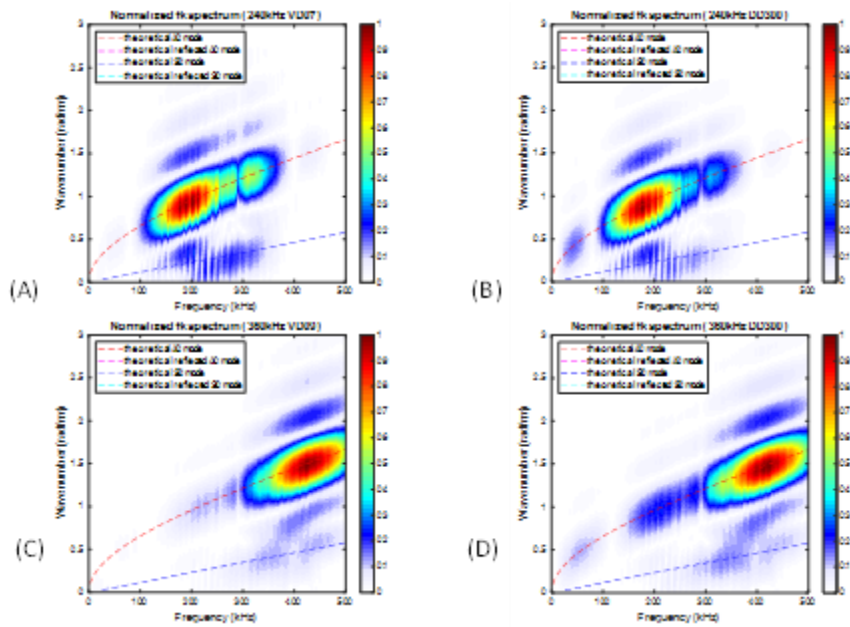


Figure 3.2 Sensing results for 240 kHz and 360 kHz PZT-SLDV tests Velocity vs. Displacement decoders. Normalized fk spectrum comparison A) 240 kHz with VD-07 B) 240 kHz with DD-300 C) 360 kHz with VD-09 D) 360 kHz with DD-300.

From the comparisons of the fk spectrums for PZT actuation that the DD-300 provides an accurate alternative to detection compared to the velocity decoders. The wavefield offers an indication that is confirmed further with the waveform comparison. It can be seen in Figure 3.4 that the displacement decoder waveform out of phase with the velocity decoder, this would be expected as when the displacement approaches a peak the velocity approaches 0. The DD-300 decoder was further verified during the investigation of complex structures in the next chapter.

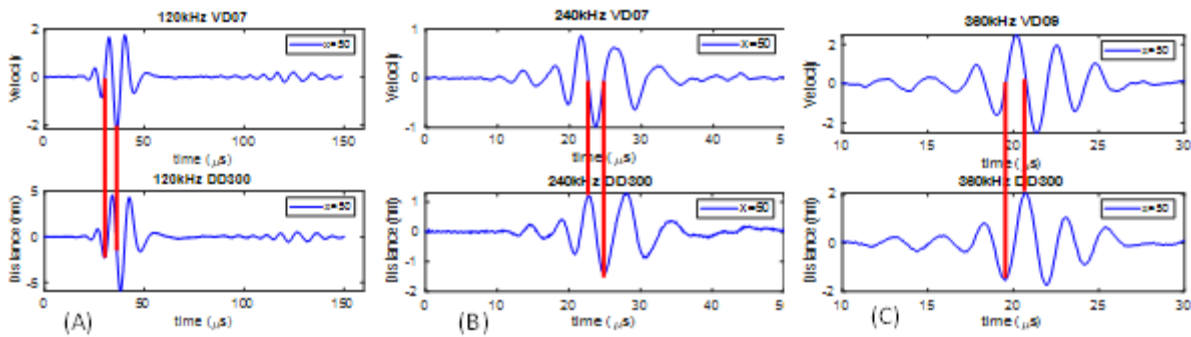


Figure 3.4 Sensing results for PZT-SLDV tests Velocity vs. Displacement decoders waveform comparison A) 120kHz VD-07 20 vs DD-300 B) 240kHz VD-07 20 vs DD-300 C) 360kHz VD-09 20 vs DD-300.

CHAPTER 4

LAMB WAVE DETECTION ON COMPLEX STRUCTURES

Lamb waves have been shown to be used for material property characterization and damage detection on plate like structures. In this chapter we aim to develop and enhance Lamb waves' ability to test complex structures such as thin foils and small diameter tubular structures. The key areas of concern for this are consistent and repeatable: A) inspection placement of the samples. B) PL actuation C) surface conditions for SLDV detection. The arrangement of recording the data from both decoders was continued and the tests in this chapter were used as further evaluation and verification of the DD-300 decoder.

We first investigate tabular structure with a diameter of 0.375" and a wall thickness of 0.035" (9.525mm and 0.889 mm respectively). To establish a constant mounting system, custom grips (Figure 4.1A) were made that lock into place on the T-slot framing. This allows the sample to be removed and replaced without requiring realignment. There is a large area that the sample can be positioned in due to the adjustability of the framing. This allows for accurate positioning for constant PL actuation on the surface of the sample, and SLDV sensing.

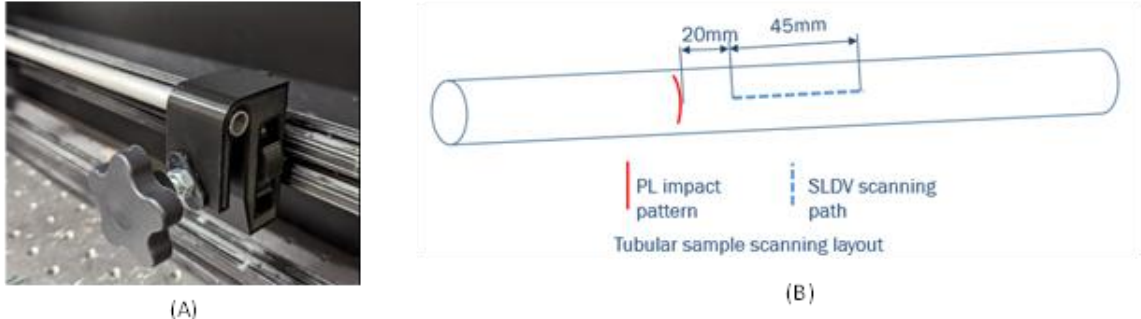


Figure 4.1 Same sided PL-SLDV testing arrangement for tubular samples A) Custom grips, B) Actuation and sensing schematic.

Considering the small size and the tubular shape of the test sample, and lab safety requirements for pulsed laser application, it was determined that same side PL-SLDV testing would be more applicable for this testing. The actuating and scanning layout can be seen in Figure 4.1B. In this arrangement we use the line focusing lens and an energy of 30 mJ to actuate a straight crested Lamb wave and perform a 40 mm line scan starting at 20 mm away from the actuation location. The first test sample used for this testing is a 2024 T3 Aluminum, Figure 4.2 shows the wavefield and $f-k$ spectrum from both the velocity, and displacement decoders. The wavefields from the displacement decoders do not show a clear dispersion within the wave packet. However, the $f-k$ spectrum indicates that the displacement decoder has not only sensed up to 4000 kHz, but that there is a clear match with the theoretical dispersion curve for a plate with the same thickness.

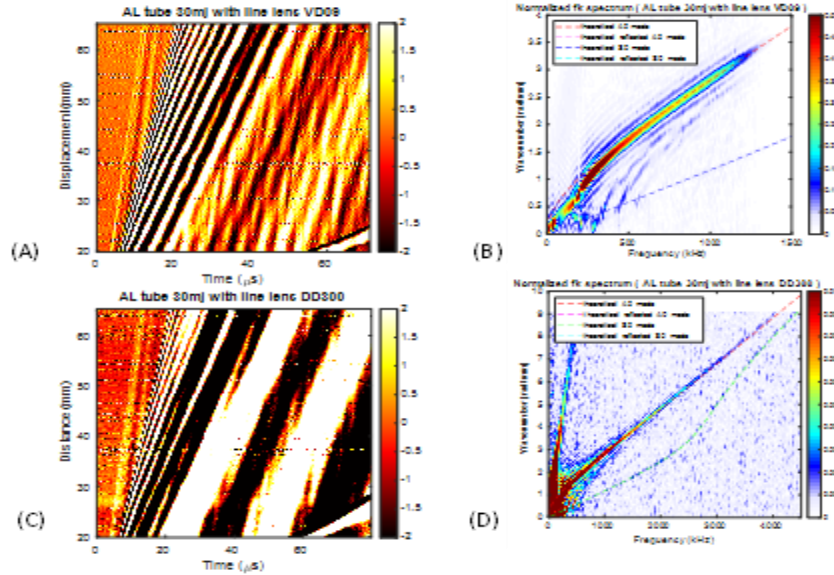


Figure 4.2 Sensing results for AL tube sample tested at 30 mJ PL-SLDV tests Velocity vs. Displacement decoders. A) VD-09 20 wavefield B) VD-09 20 fk Spectrum C) DD-300 wavefield D) DD-300 fk Spectrum.

To further explore this tubular structure and the ability of the Lamb waves NDE for evaluating different materials, a second sample of 304 stainless steel had an aluminum foil tape applied to enhance the PL actuation [1], as well as using a reflective tape was used to improve the signal received by the SLDV system. Figure 4.3 shows the wavefield and fk spectrum from both the velocity and displacement decoders. Note the waveforms both have a lower amount of noise, however the displacement measurement still lacks the clear wave packet of the velocity. The fk analysis of this test indicates that while the high frequency component (higher than 2000 kHz) of the A0 mode is not seen, 2 additional modes, S0 and A1 are seen at frequencies up to 3500 kHz using the displacement measurement. It is noted that the addition of the reflective tape has affected the fitment of

the dispersion curves to the theory; this is an indication of the sensitivity that this system has for thickness detection.

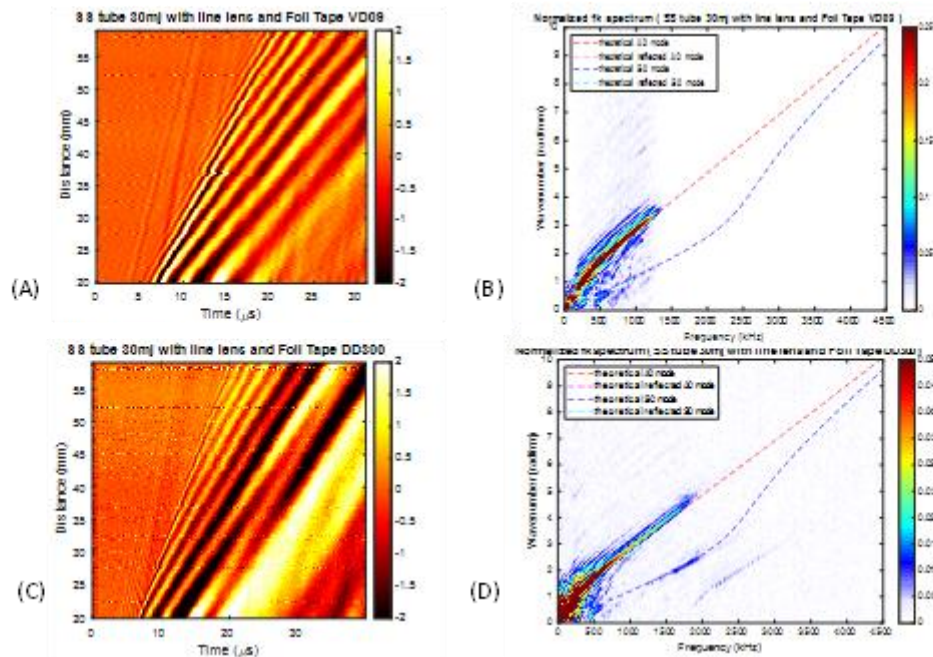


Figure 4.3 Sensing results for SS tube sample tested at 30 mJ PL-SLDV tests Velocity vs. Displacement decoders. A) VD-09 20 wavefield B) VD-09 20 fk Spectrum C) DD-300 wavefield D) DD-300 fk Spectrum.

The study of thickness measurement of thin foils began with a 76 μm Aluminum foil that is 150 mm wide and approximately 400 mm long. Using the same side inspection, while recording both velocity and displacement measurements. The energy level was reduced to 3.9 mJ with the line lens and the spatial resolution was increased to 0.2 mm. To hold the sample with a consistent surface for actuation and sensing, a pair of 3D printed grips were constructed to hold the sample from the short sides and apply a small amount of tension to hold the sample smooth (shown in Figure 4.4A). The sensing schematic for these tests is shown in Figure 4.4B, starting at 5 mm away from the actuation line and continuing to 40mm away.

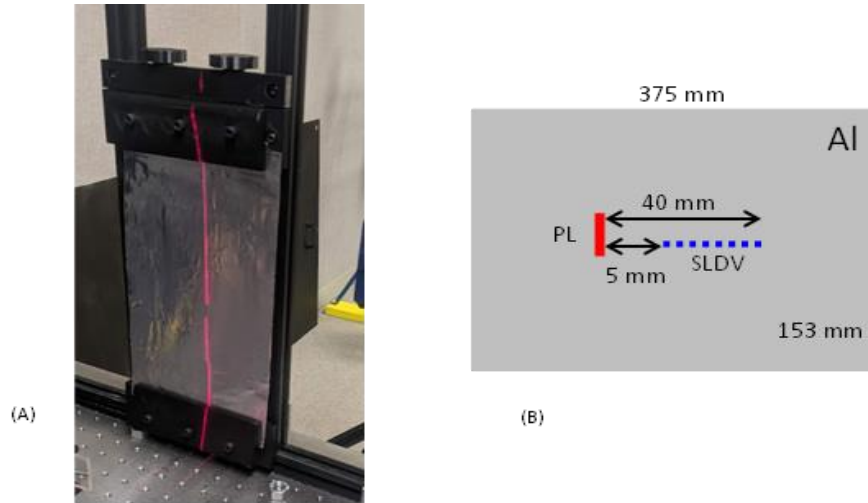


Figure 4.4 Thin foil PL-SLDV testing A) gripping solution. B) Actuation and sensing schematic.

The results from this test are shown in Figure 4.5. Both decoders have a large amount of noise in the wavefield, however the fk analysis shows that there is a clear agreement with the theoretical curves. It is noted that in this test the VD-09 200 decoder reached its maximum frequency of 2.5 MHz, while the DD-300 decoder reached the maximum wavenumber achieved by our testing configuration.

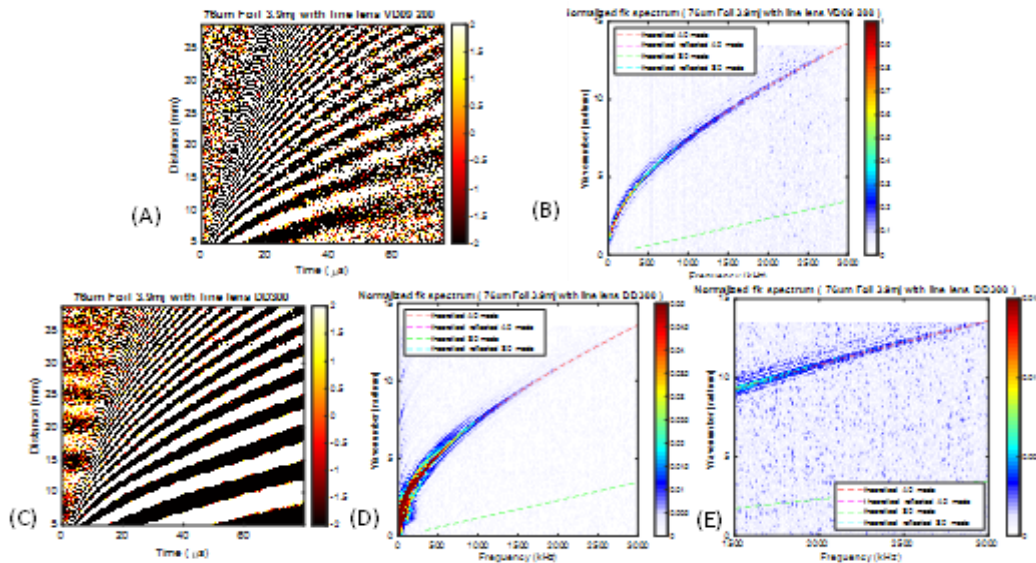


Figure 4.5 76 μm Al foil sample tested at 30 mJ A) VD-09 200 wavefield B) VD-09 200 fk Spectrum C) DD-300 wavefield D) DD-300 fk Spectrum E) DD-300 fk Spectrum from 1500 to 3000 kHz decreased colormap.

25.4 μm Al foil was tested using this configuration, and the results are shown in Figure 4.6. The noise level in the wavefields is very high, but the fk analysis shows that a dispersion curve was detected by both decoders. In this test VD-09 200 had a much higher amount of noise, however the DD-300 clearly shows the curve to the maximum wavenumber.

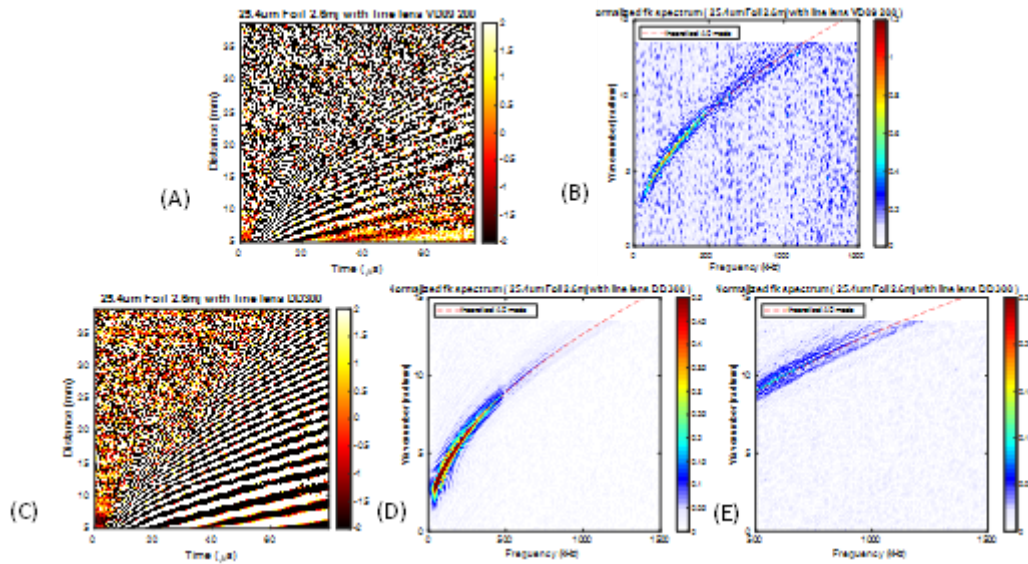


Figure 4.6 25.4 μm Al foil sample tested at 30 mJ A) VD-09 200 wavefield B) VD-09 200 fk Spectrum C) DD-300 wavefield D) DD-300 fk Spectrum E) DD-300 fk Spectrum from 1500 to 3000 kHz decreased colormap.

CHAPTER 5

PART I CONCLUSION

The comparison of test performed with the fully non contacting PL-SLDV system, and the tests on complex structures, have proven that we have successfully established a testing configuration suitable for testing when access to one or both sides is available. Based on testing with the PZT-SLDV system and the PL-SLDV system the DD-300 displacement decoder has been proven to be a viable alternative to the convictional velocity decoder options. The DD-300 decoder has been shown to be capable of detection up to 4Mhz. Despite the large amount of noise and interferences seen in the measurements, the frequency wavenumber analysis revealed the dispersion curves and achieved the thickness measurement, demonstrating robustness in the use of displacement measurements. The same side PL-SLDV system has shown that the theoretical dispersion curves developed for plate like structures can be applied to a small diameter tube, and the tubular structure has had no discernible impact on the fk analysis. The same side PL-SLDV system with the DD-300 decoder has shown the ability to actuate and detect Lamb waves on foils as thin as 25.4 μm . It is the recommendation from the author that future work include: A) continued verification of the theoretical lamb wave dispersion curve models, and the DD-300 decoder above 4 MHz, B) an investigation into methods to reduce the spatial resolution below 0.2 mm to increase the maximum wavenumber seen in the fk analysis, C) studies into the detection of coating thickness with a variety of coating materials such as gold and chromium.

CHAPTER 6 PART II

CRACK MITIGATION USING ENGINEERED COMPOSITE PATCH

As stated earlier in the thesis, NDE has focused on defects such as crack detection. Less attention has been given to the needs after the cracks are identified. Industries such as the nuclear industry are seeking mitigation methods when the cracks are detected for safety insurance. Nuclear spent fuel canisters have been designed and used for nuclear waste storage since the 1950's and placed largely in near-marine environments [7,8]. Welded stainless steel (SS) have been widely used for dry spent fuel storage and placed in the ventilated storage system at sites near coastal region for cooling down the waste. Dust and sea salt are carried by the air flow of the ventilation system and adhered to the surface of the canisters. As the temperature around the canisters cools down over time, sea salts on the surface will deliquesce to form brine, which forms a humid and corrosive environment [8,9]. The process of welding applied to the canisters during manufacturing results in residual stresses in the heat-affected zone (HAZ) [10,11]. Stress corrosion cracking (SCC) thus tends to occur under such corrosive chemical conditions and around areas subject to residual stress [12,13]. Combining with other factors such as ambient temperature, materials composition/microstructure, and other external stresses [11]. In the chloride-rich costal environment, chloride-induced SCC

(CISCC) often occurs along the welded regions or HAZ of the canisters and degrades the stainless steel.

Welded stainless steels (SS) such as SS 304, SS 304L, SS 316, SS 316L, or SS 316LN [8,13] have been widely used for dry spent fuel storage. The letter "L" stands for "low carbon" content in the steel and letter "N" stands for nitrogen to compensate for the loss of steel strength. 316 SS has molybdenum (Mo) added to increase resistance of chloride induced corrosion as compared to 304 SS. In our studies we focused our efforts on SS 304. Fiber reinforced polymer (FRP) materials including carbon FRP (CFRP), and glass FRP (GFRP) have been used for retrofitting steel and/or aluminum structures [14,15] such as buildings, aircrafts, and bridges. FRP composites have a high strength-to-weight ratio, and the capability of corrosion resistance [16], and high durability [17]. Regarding the performance of FRPs in the presence of moisture, E. P. Douglas et. La. [18] report that water molecules or moisture could potentially penetrate the composite materials via diffusion and affect the structure system. [19] adds that the porous structure of the epoxy molecular network may also act as a pathway for moisture that can affect the structure system.

Once a CFRP is bonded to a flawed structure, it has been shown to slow crack propagation by bridging CFRP materials across existing cracks and reducing crack opening and crack tip stress [20]. The thickness of the applied adhesives plays an important role because it impacts the shear and peeling strength when subjecting the patched system to its working environment with various mechanical loading [21]. For example, investigators have studied: A) a relatively thick adhesive layer (> 0.25 mm), B)

a non-conductive layer and C) a GFRP layer, concluding that such layers appear to slow or prevent various forms of corrosion [22].

In response to the needs for crack mitigation, Part II of the thesis is focused on the development and evaluation on an engineered carbon fiber reinforced patch mitigation method that is designed to impede the growth of these SCCs in the near costal region environment. The patch design criteria and guidelines including the adhesive layer parameters are learned through extensive literature studies and the learned best practices are adopted for the subject patch application in this thesis.

As patch integrity and adhesion strength are key to the success of using a patch as a method for crack mitigation, it is important to understand how various factors may affect their performances. Based on the previous work discussed, this study will take the following key parameters into consideration for creating a firm bond: A) The design of the CFRP geometry because it needs to meet the criteria that influence structure integrity and robustness. B) The selection of a proper adhesive thickness, to facilitate reducing the mechanical stress at the tip, and reduce the likelihood of chemical corrosion. As the bonding adhesive is likely affected by corrosive environment, it is necessary to first evaluate the structure integrity at room temperature and humidity then after exposure to corrosive environments.

CHAPTER 7

PATCH DESIGN AND INSTALLATION

Key factors affecting the performance of a bonded patch include: A) patch configuration, B) patch geometry, C) patch thickness. Since numerous studies on patch configuration (unidirectional (0°) or knitted woven (0°/90°)) [22,24] regarding lifetime of patched steel structure have been conducted. Following the recommendations from reference [15] for the general designs of the patch and patch adhesion, we selected unidirectional configuration of CFRP with the fiber direction aligned with the load direction for our initial investigation. The dimensions of CFRP patches should be at least 4 to 5 times the length of the crack. Equation (1) and (2) [15] are used for determining the desired patch thickness in aircraft structures. It expresses the relationship between the host metallic substrate and the CFRP in terms of the product of the Young's modulus and the thickness.

$$E_{ptp} = ERtR \quad (1)$$

$$1.6 \geq SR = ERtR / E_{ptp} \geq 1 \quad (2)$$

Where E_p and t_p are the Young's modulus and thickness of the metallic host plate, and E_R and t_R are the equivalent Young's modulus and thickness of the patch perpendicular to the crack material. The Stiffness Ratio (SR), which is the ratio of the stiffness of patch perpendicular to the crack ($ERtR$) to that of substrate (E_{ptp}) is

recommended to be within the ranges of 1 to 1.6 [23], as shown in equation (2). Based on these equations with the selection of unidirectional CFRP, if the longitudinal elastic modulus of the patch is similar to that of the host plate the recommend patch thickness would be about the same thickness of the host.

However, since the steel used in spent fuel storage canister system can be thicker (> 10 mm) than the steel plates used in typical laboratory testing, selecting a patch thickness for our baseline studies that is close to the recommended value is difficult. In this thesis, CFRP composites with thicknesses of 0.15 mm and 0.3 mm are selected for use on a 0.91mm thick steel plate to investigate and improve our understanding of the correlation between CFRP composite patch thickness and specimen response.

In addition to patch geometry, the effect of adhesive layer thickness on CFRP/adhesive/steel specimen response is investigated. Previous studies [25] have shown that the adhesive thickness affects bond performance under tensile loading, with [21] suggesting thickness range of adhesive between CFRP layer and the steel substrate to be 0.5 – 2 mm. This recommendation is contrasted by the manufacturer of the epoxies selected in this work that call for a layer thickness of between 0.05mm and 0.1mm [26]. Since the thickness of the steel specimens was 0.91 mm, adhesive thicknesses above 0.5 mm were not considered in this work.

The selection of the CFRP was investigated first. Most unidirectional CFRP composites possess similar or even greater strength than steel in the fiber direction (longitudinal direction), while the woven CFRP composites possess moderate strength along the fiber direction. In the transverse direction, the strength of unidirectional CFRP

composites is often lower than those of CFRP composites with woven structure. In this study, unidirectional CFRP composites with different thicknesses were selected to study the effect of patch thickness and adhesive thickness. The effect of CFRP configuration and adhesive would be investigated in future studies to understand the correlation among patch configuration, residual load, and extreme environment.

7.1 MATERIAL SELECTION AND PREPARATION

The steel used in the study is SS 304. The samples are prepared as small plate-like test pieces that will fit into an MTS test frame. Prior to discussing the sample preparation procedure, a previous study regarding composite application to steel components is noted [16]. In this work, the author discussed a general method of FRP patching, which includes surface preparation by sanding with a mild abrasive and cleaning with acetone. Once the steel specimen surface was prepared, a viscous, two-part epoxy was used to bond the CFRP while ensuring that the carbon and steel are not in direct contact to minimize the potential for galvanic corrosion.

Preliminary 304 SS samples were manufactured with a thickness of about 0.91 mm and 50 mm by 150 mm dimension. Initial testing of the 304 SS material indicated that $E = 193$ GPa. For use with the steel specimens, three types of CFRP composites were selected and are shown in Figure 7.1. The composites are: A) unidirectional carbon fiber pre-impregnated (prepreg) films supplied by Rock West Composites, USA with thickness of 0.15 mm and a reported $E = 241$ GPa, B) unidirectional carbon fiber film supplied by Fibre Glast, USA with a quilted banding pattern, thickness of 0.3 mm and $E = 257$ GPa, and C) unidirectional carbon fiber film supplied by Fibre Glast, USA with a lateral

banding pattern, thickness of 0.3 mm and $E = 257$ GPa. The composition of the unidirectional CFRP prepregs have up to 93% carbon fiber

The patches were then bonded to steel specimens using the procedures outlined in previous study [16] with the fibers in the longitudinal direction, parallel to the length of the specimen, and in the loading direction. Using equation (2), the SR for each patch 0.21 for the composite in A) and 0.44 for the composite films described in (B, C). These three composites were compared using a preliminary testing method, and it was decided to focus further studies on the use of CFRP in A) since it incurred the largest axial load.

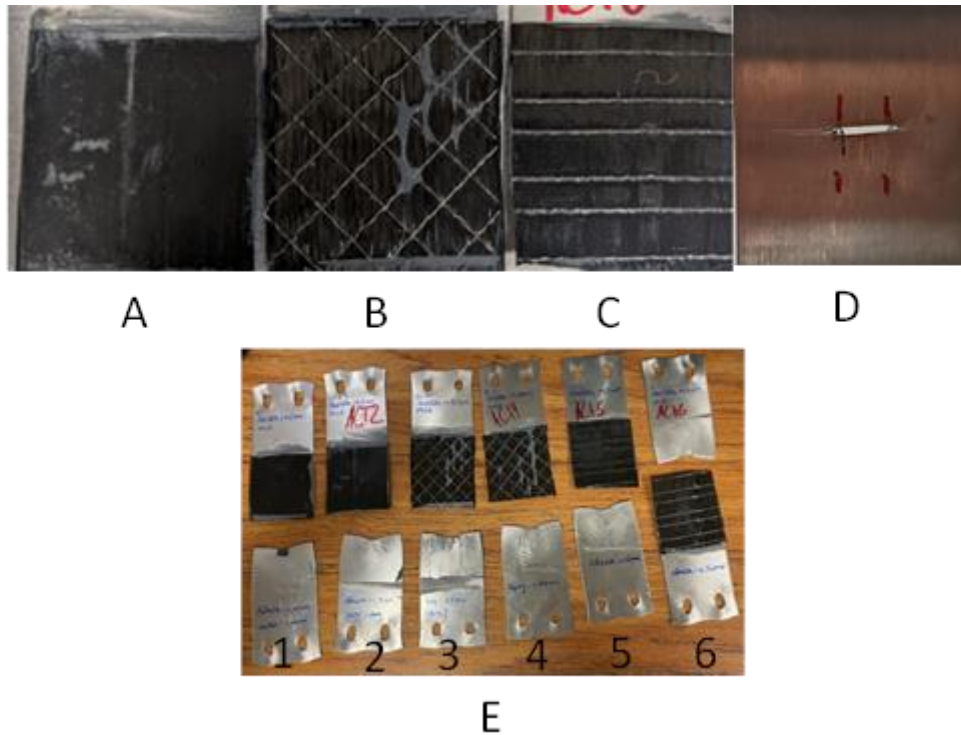


Figure 7.1 Patch types after bonding, A) Rock West Prepreg, B) Fibre Glast plain unidirectional type 1, C) Fibre Glast plain unidirectional type 2, D) Control, E) Preliminary test samples 1- 6 going from left to right.

7.2 ADHESIVE THICKNESS AND UNIFORMITY CONTROL

For the preliminary tests, Huntsman Araldite 2013-1 epoxy adhesive was used, and It was decided to continue the patch design using the Rock West Prepreg due to it having the highest max loading during testing. The Huntsman Araldite 2013-1 epoxy adhesive (Perigee Direct, USA) is a 2-Part mixture at 1 to 1 ratio, and room-temperature-curing adhesive which claims good chemical resistance and high strength. Araldite 2013-1 has a glass transition temperature (T_g) of around 66.7°C when curing at 25°C for 24 hr. and a maximum elongation of 1.8%, and a recommended thickness range from 0.05 mm to 0.1 mm.

To ensure that the patch has uniform mechanical properties, the thickness and uniformity of the patch are critical. Because of the size of the desired patch and the ongoing development of the patch, it was cost effective to use Fused Deposition Modeling (FDM), opposed to conventional manufacturing methods. Creo Parametric, a 3D modeling software was used to design a 3-part model for applying pressure onto the patch-applied steel structure to create an even patch surface. Figure 7.2A shows a prototype mold that was built to demonstrate the feasibility of the adhesive mold: it consists of a main body, a bolt, and interchangeable pressure plates with a stopper depth of 0.65 mm, as shown. The main body supports the patch-applied samples when the samples are inserted in the gaps between the pressure plates and the main body. Then the bolt can be tightened to apply load to the patch surface via the pressure plates. The 50 mm by 50 mm contact area of the interchangeable pressure plates have different depth stops for distributing the pressure evenly across the patch surface and control the

thickness by limiting the travel of the pressure plates. The excess adhesive can be easily cleaned after pressing. This design was later refined to accept the 75 mm wide sample.

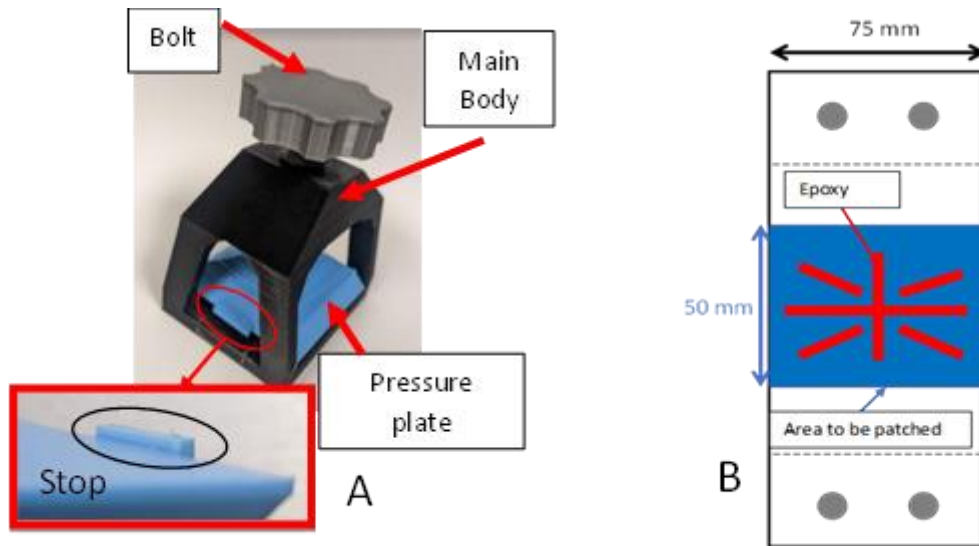


Figure 7.2 A) 3D printed Proof-of-concept prototype adhesive mold. B) Illustration of adhesive application pattern. A 75 mm by 50 mm CFRP composite.

The average thickness was then calculated by measuring the thicknesses of the 4 corners and the thickness of the middle for each fully cured sample. Although an even patch surface with targeted adhesive thickness can be achieved with the 3D printed adhesive mold, the uniformity of the adhesive layer needs to be inspected using the methods developed previously to determine if air-bubbles formed. A star like pattern of epoxy shown in Figure 7.2B is used to help reduce the likelihood of trapping air-bubbles. The author notes that one approach to adhesive thickness control that has been tested is achieved by mixing the adhesive with steel balls [27] or non-metallic spacer beads [21], and firmly pressing or clamping the patch-applied steel structure.

7.3 PRELIMINARY SAMPLE DESIGN

The preliminary sample design was heavily influenced by the grips required for the selected testing equipment, this led to a 50 mm (1.96 in) wide by a 150 mm (5.90 in) long sample with 6mm mounting holes to match that of the grips. This basic sample shape was used with two different crack starter geometries: A) one 3mm hole and B) a 10 mm by 1 mm slit both centered on the sample shown in Figure 7.3. These samples were made from 1mm thick 304 stainless with crack starters being machined by one of the school's machine shops.

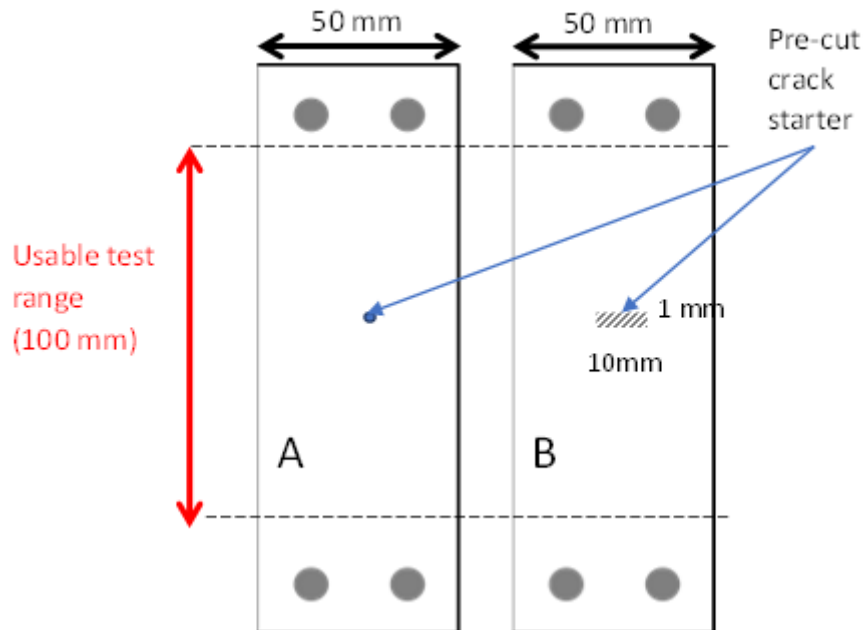


Figure 7.3 Preliminary test sample geometry. A) 3 mm hole B) 10 mm slot.

7.4 PATCH APPLICATION PROCEDURE

The surface preparation performed as a part of the manufacturing process was excluded in our surface preparation processes because the as-received SS plate is a pristine plate without paint, rust, or inactive oxide layers. The patch application process begins with surface preparation, 150-grit sandpaper was used to promote epoxy bonding. The plate is then cleaned with acetone to remove oil/grease, sanding particulates, and any

organic contamination. Due to our testing sample design, a small piece of tape is applied to the back side to prevent epoxy leaking. The Loctite High Heat epoxy was mixed using the static mixing tube and applied in a star-like pattern (Figure 7.2B). Then the composite layer was placed onto the epoxy. Then, the patch-installed samples were inserted and pressed with a 3D printed adhesive mold. The excessive adhesive allowed to flow out due to the pressing was cleaned. Last, the samples were air-dried at ambient condition (room temperature ~70 F and humidity~30%) for a minimum of 36 hours before conducting experiments.

CHAPTER 8

PATCH STRENGTH AND REPAIRING EVALUATION

For the composite patch, it is critical to ensure secure adhesion between the patch and the plate. In this chapter a testing procedure that can test the effective strength and repairing capability of a carbon composite patch by controlled crack growth in a stainless-steel plate is explored. This goal was divided into three subsections: A) establishing a testing plan and procedure, B) sample design, C) patched sample testing.

8.1 TEST DESIGN

There are multiple methods by which a crack can be generated in a test sample, such as corrosion, fatigue, and tensile loading. It was decided to pursue a uniaxial tension test to evaluate the change in strength of the sample that comes from the patching process. A preliminary sample size of 50 mm wide and 150 mm long was used. This size was decided upon because it offered enough surface area for patch attachment, while keeping the cross-sectional area to a minimum making crack production faster. The testing equipment that was available and capable of handling our relatively small sample size is the MTS 810 (Figure 8.1A). This system uses the MTX 458.20 microcontroller, with a 458.11 DC Controller used for Load control, and a 458.90 function generator to create the loading signal (Figure 8.1B). The associated data acquisition system was used to record the load, as the displacement was controlled. The data acquisition system was set to start recording data at 40 lbf and to trigger the end of test when load falls below 5

lbf. The displacement was set to increase one thousandth of an inch per second (0.0254 mm/s).

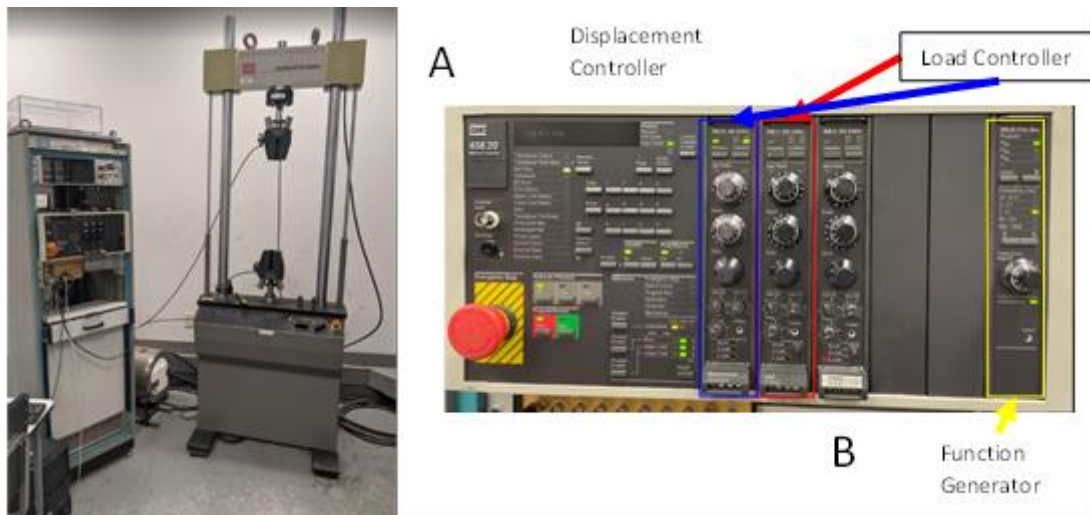


Figure 8.1 Selected testing equipment A) MTS 810 Material Testing System B) MTX 458.20 Microcontroller.

To utilize this system while testing 304 stainless steel, custom grips had to be made. The design requirements for these grips were to have a $\frac{3}{4}$ -10 threaded hole that matches the attachment method on the system, and a method of clamping down on the stainless-steel sample. To ensure that there is even distribution of clamping load, two $\frac{1}{4}$ -20 bolts were used with a clamping area of 1" by 2", shown in **Error! Reference source not found.A**. These designs were created using Creo Parametric, and then sent to the machine shop to be made from A36 Carbon steel. This design went through a few changes as testing continued, these revisions were targeted to create a slip free uniform grip on the test sample. The first revision addressed the smooth mounting surface, by adding a 0.015" machined pattern cut into each face of the grips to so that when tightened the grips would embed a small amount limiting the ability to move or slip. **Error! Reference source not found.B** the evidence of slippage and uneven load application.

The final revision of the grips seen in **Error! Reference source not found.**C came after many attempts to find a sample design suitable for the original grips. In this revision the bolts were enlarged from 1/4-20 to 7/16-14 hardened chromoly bolts. The bolt spacing was increased from 1" to 1.1875" to accommodate the larger bolts, and finally the clamping

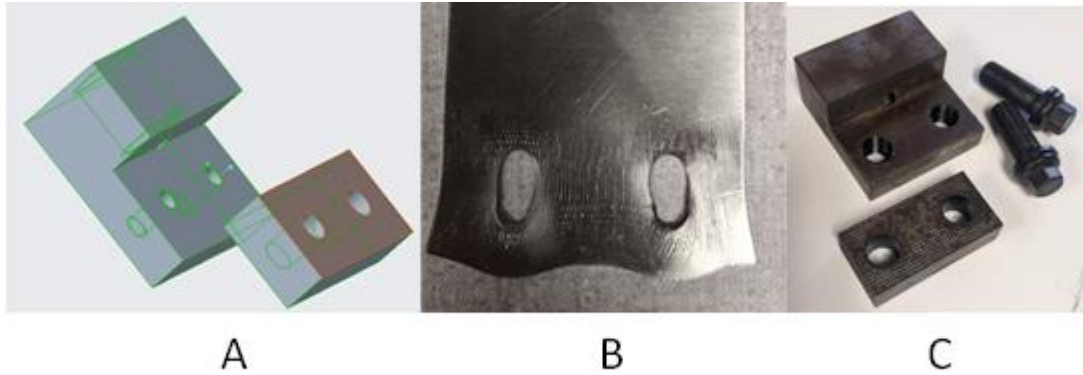


Figure 8.2 A) 3D model of original grip design sent to machine shop. B) evidence of slippage C) Final Grip jaw were hardened to increase its strength.

8.2 STRESS CONCENTRATION STUDY FOR LOADING TEST DESIGN

These preliminary crack samples were loaded in tension until failure. Results from these tests indicated that the stress concentrations were not suited to ensure that failure occurred at the center, as in both cases the samples failed at one of the mounting bolts. A stress concentration study was performed on our test samples, and new sample designs using the Creo suite of software licensed through the university. The sample design had limitations applied to it for a variety of reasons. The key criteria were that: A) the grips were made and having new ones manufactured would increase time delays and cost, B) the surface area for the patch attachment needed to remain as large as possible,

C) the crack starter needs to have the largest difference in stress concentration as possible.

A base model of the preliminary sample size was created so that the crack starter geometry could be modified simply. Figure 8.3 gives examples of the various sample geometries that were tested. The samples highlighted are V1 which has a 3 mm hole at the center, V3 a dog bone shape that reduces to 40 mm wide at the center, V6 the same as Sample B from the preliminary testing with 1mm wide 10 mm long slot made at the center, V9 shows a look into the effects of having an edge crack starter for possible future work, and finally V15 is a combination of the 3 mm hole and a 10 mm x 1 mm slot.

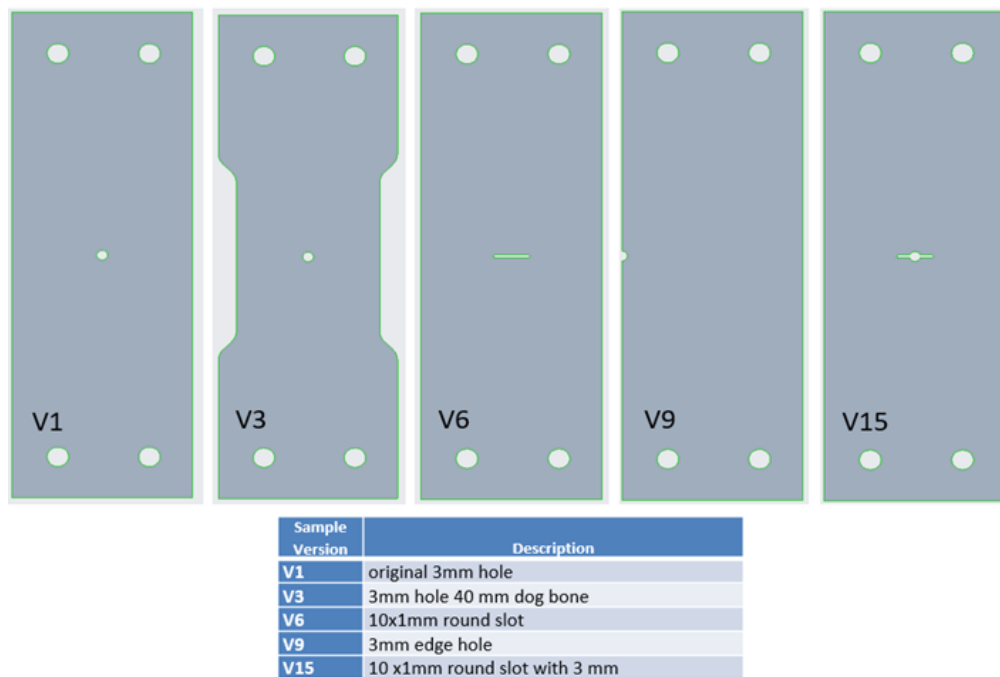


Figure 8.3 Examples of sample designs used in stress concentration study with descriptions.

With the models created the simulation that was ran was a simple tension loading case where a 2000 lbf load was placed on the mounting holes, shown in Figure 8.4A. This loading was assigned to simulate a worse case where the gripping surfaces offer no load dispersion, and all the load is applied directly to the mounting holes.

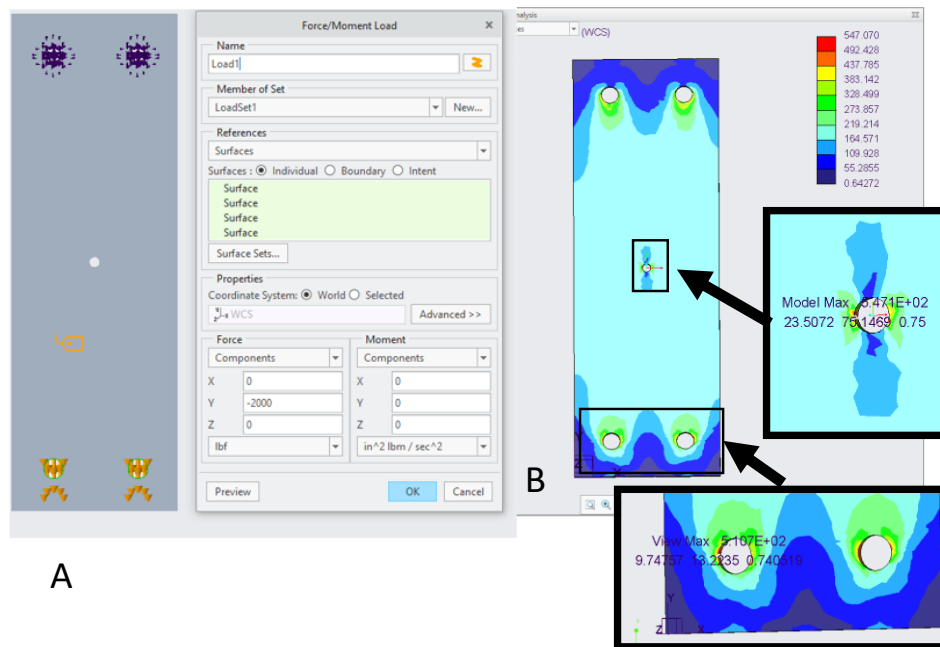


Figure 8.4 A) Example of simulation loading B) Example of stress concentration colormap of sample V1.

The simulation used the material properties of our 304 stainless steel, and a finite element method of analysis was to calculate the resulting stress, strain, and displacement of each sample design. This model was run to a maximum of 9 iterations or to a convergence of 10%. The convergence is met when there was less than 10% change in the results between the current and last iterations results. All the model simulations were run with the same loading and analysis setting, so the comparison between the max Von Mises stress seen on each sample can be compared with the higher stress meaning that

the geometry would be more favorable. Table 8.1 shows the name, description and max stress of each sample is reported in MPa.

As a result of the mounting geometry that the grips have, all the models saw a stress concentration at the mounting points, this is shown in Figure 8.4B. Sample V1 is shown to have max stress Von Mises of 547.07 MPa, while this is above the ultimate tensile strength of 515 MPa the mounting holes also experienced a stress of 510 MPa indicating that failure is likely to occur at the center, however there would be a large amount of deformation at the ends, and testing would be very difficult to get consistent results. As each sample geometry was processed it became clear that the stress at the mounting points was consistently the same because the local geometry did not change. The list of tested samples can be seen in Table 8.1

Table 8.1 Tested samples and their resulting max stresses.

Sample Version	Description	Max Stress Von Mises (MPa)
V1	original 3mm hole	547.07
V2	6mm hole	559.046
V3	3mm hole 40 mm dog bone	630.481
V4	3mm hole 35 mm dog bone	794.817
V5	9mm hole	579.314
V6	10x1mm round slot	1357.54
V7	10x1mm sharp slot	1234.87
V8	10x2mm round slot	964.442
V9	3mm edge hole	536.915
V10	5x1mm edge round slot	1589.9
V11	5x2mm edge round slot	1236.33
V12	5x1mm edge sharp slot	1570.51
V13	5x.5mm edge round slot	2376.77
V14	5x.1mm edge round slot	4811.55
V15	10 x1mm round slot with 3 mm	1419.84
V16	5 x1mm round slot to one side with 3 mm	1129.78
V17	10 x.5mm round slot with 3 mm hole	2011.73

V18	40mm dog bone with 10 x1mm round slot with 3 mm hole	1961.49
V19	40mm dog bone with 10 x1mm round slot	1754.58
V20	10 x.2mm round slot with 2 mm hole	3238.10

A successful improvement of the design was characterized by a significant increase in the difference in the maximum Von Mises stress of the sample compared to the maximum seen at the mounting holes. The design of sample V20 calls for an overall sample size of 50 mm by 150 mm, with a 2 mm hole drilled at the center, that is

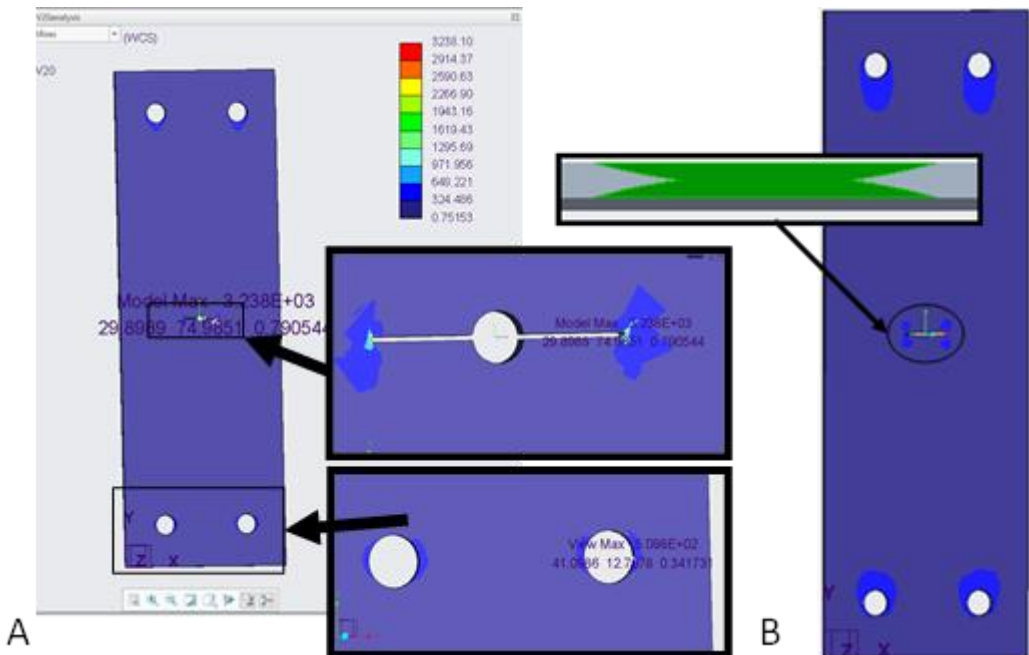


Figure 8.5 Stress concentration study results A) Sample V20 B) Final selected crack starter geometry. intersected by a 0.2 mm by 10 mm slot. As seen in the load simulation in Figure 8.5A the maximum Von Mises stress of this sample when loaded with 2000 lbf is 3238.1 MPa.

After discussion with multiple machine shops locally only one was found that had the capability to manufacture test samples of design V20. This sample was designed with

the intent of using Electrical Discharge Machining (EDM) to make the 0.2 mm cut. The EDM process can be performed when cuts have small dimensions, with tight tolerances. This process requires specialized equipment, and trained professionals, that the machine shop on campus does not have, therefore we approached a few local shops to inquire about their ability to produce our samples. Due to a high-cost estimate from local machinist, the sample design was revisited, and alternative methods of manufacturing were explored. The goal for this optimization process is to find a sample geometry and manufacturing method that will be more cost-effective to manufacture in large numbers, while also retaining a similar stress concentration. Sample V23, Figure 8.5B is based on using a small diameter cutting tool to make a cut from both sides so that the opening created by the overlap is 10 mm in length. Sample V24 uses the same cross-sectional geometry as V23 however the corners rounded to represent the cutting edge of an abrasive cutting wheel. Sample V24 was selected for further preliminary testing because it offers a high stress concentration and is possible to be made in the lab with nonspecialized tooling. Table 8.2 offers a list of the newly attempted sample geometries and their results.

Table 8.2 Redesigned test samples and stress concentration results.

Sample Version	Description	Max Stress Von Mises (MPa)
V20	10 x.2mm round slot with 2 mm hole	3238.10
V21 A	60 Degree point cut 5mm in from both sides	891.28
V21 B	20 Degree point cut 5mm in from both sides	976.51
V21 C	45 Degree point cut 5mm in from both sides	818.75
V22	20 Degree point cut 10mm in from one side	1175.53
V23	A 38.1 mm abrasive wheel used to cut a 10 mm wide slit BASIC	2296.60
V24	A 38.1 mm abrasive wheel used to cut a 10 mm wide slit REALISTIC	5291.81

Samples V23 and V24 were designed with the idea of using a small handheld cutting tool. For the simulation a cutting disc for Dremel, a popular well-known brand, was used because it offered an advertised cutting thickness of only 0.6 mm and a radius of 38.1. From the previous simulation results it was clear that the thinner the cut the larger the stress riser. Due to the radius of the cutting disc the sample had to be cut from both sides to ensure that the stress riser is centered in the sample, and the damage caused by the radius of the disc was kept to a minimum. After the simulation was complete and the sample geometry selected, the Dremel model 4300 76-piece kit shown in Figure 8.6A was used for sample production. The first cuts using the new Dremel revealed that a jig to assist with the positioning of the cutting tool making each cut more consistent and repeatable was needed. This system shown in Figure 8.6B was 3D printed so that it could be altered and refined quickly. Several samples were then made and used for preliminary test.



Figure 8.6 Tools used for crack starter cutting A) Dremel model 4300 76-piece variable speed corded multipurpose rotary tool with hard case purchased from Lowes.[28] (B, top and bottom) Sample cutting jig made of Blue PLA.

8.3 UNIAXIAL LOADING TESTS FOR BONDED PATCH EVALUATION

The first uniaxial tension test was conducted using the selected geometry, and the proposed method of patching. These tests were to serve as proof of concept for the loading system and data acquisition system, while also giving an initial impression of the patching method. The testing procedure was to load the sample into the system while the displacement was at 0, then the displacement was increased at a rate of 0.001” per second, until complete failure occurs. Figure 8.7A-B shows the test sample before and after testing. Graph 8.2 shows the load vs displacement for the 3 unpatched samples used to establish a baseline. Graph 8.1 shows the load vs displacement for 2 samples that were patched using the method developed previously. These tests highlighted a problem shown in Figure 8.7C with the grips that the mounting holes are deforming under loading. This yielding is not controlled or accounted for in the patch, and therefore creates concerns of

consistency. Because of this yielding the grips were changed to a larger bolt size spaced further apart. To accommodate this change, we increased the sample width from 50 mm to 75 mm, and increased the hole size from 6 mm to 12 mm. Figure 8.8A is a schematic of the final test sample design, and B shows a sample mounted for testing, and C Shows a patched sample ready for testing.

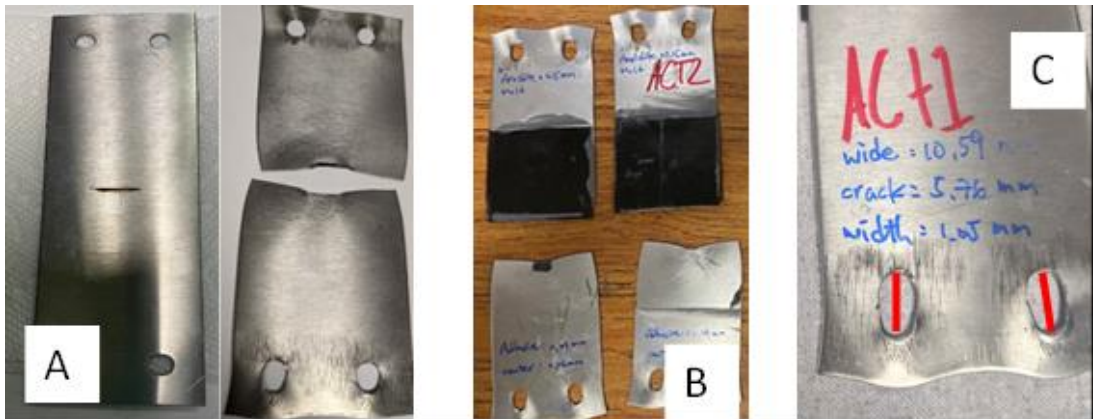
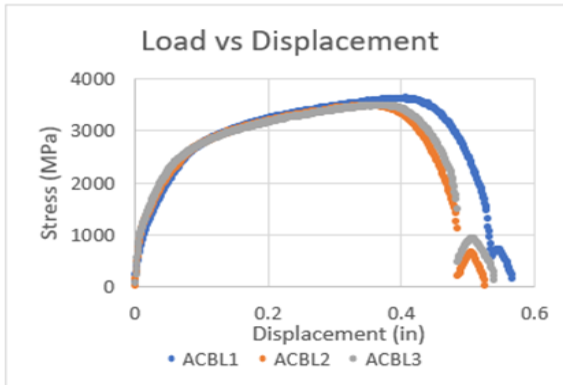
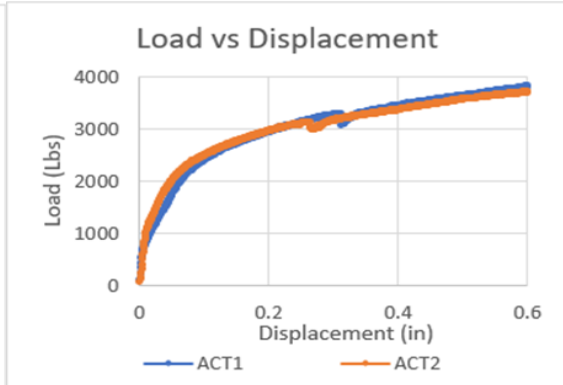


Figure 8.7 A) Control test sample #1 before and after testing B) Patched test sample #1 before and after testing C) Close up on deformation seen on baseline test 3 and Patch Test 1.



Graph 8.2 Control Results



Graph 8.1 Group 1 Results

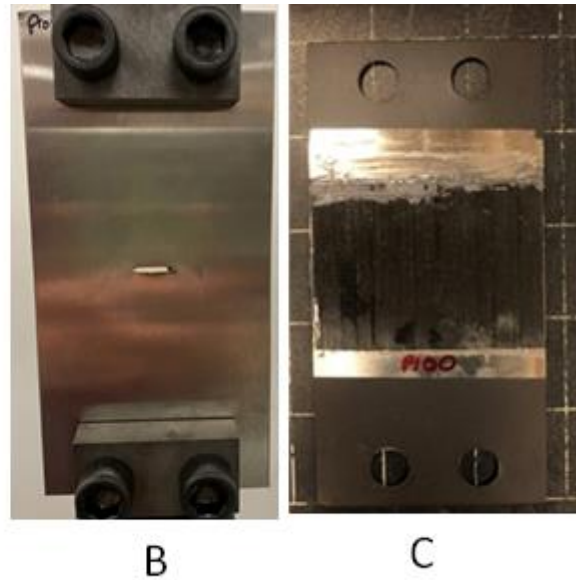
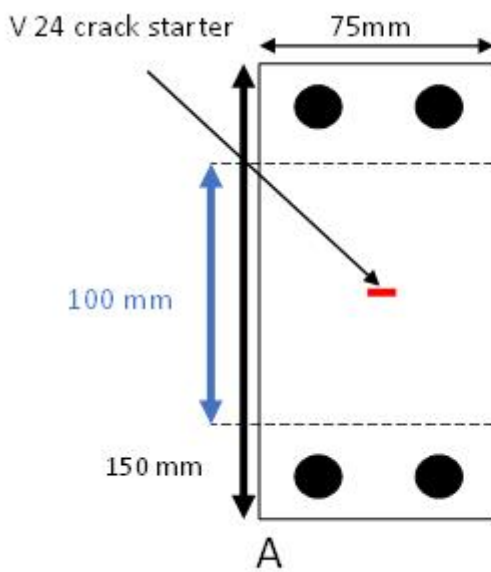
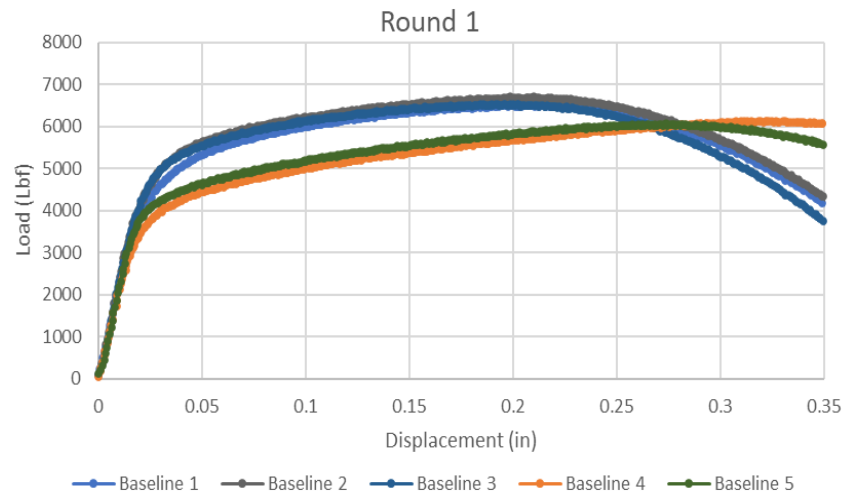


Figure 8.8 A) Final tension testing sample design B) Final test sample loaded for testing C) Final Patched test sample.

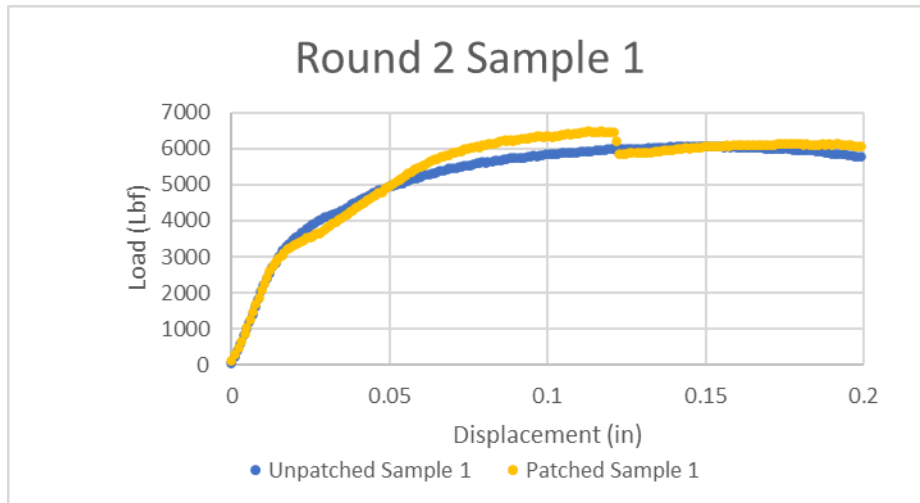
When evaluating the effectiveness of our patch multiple rounds of testing were conducted and compared using the plots of the load in lbf vs. the displacement in inches. The results from the unpatched samples in the first round of testing is shown in Graph 8.3. The large difference between tests 1-3 and tests 4-5 raised concerns for our testing method, however it was determined that samples 4 and 5 were made from a different SS plate than samples 1-3. Due to this vast difference in results, in round 2 each plate that

was used to make samples had samples that were patched and unpatched for a constant comparison. Ultimately it was determined that all samples for each round of testing would be made from the same sheet to completely remove this.

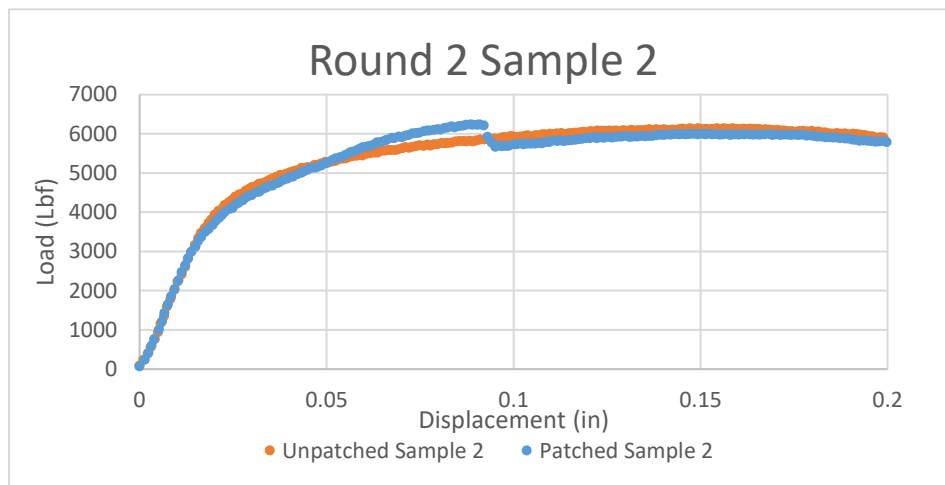


Graph 8.3 Round 1 Unpatched samples only

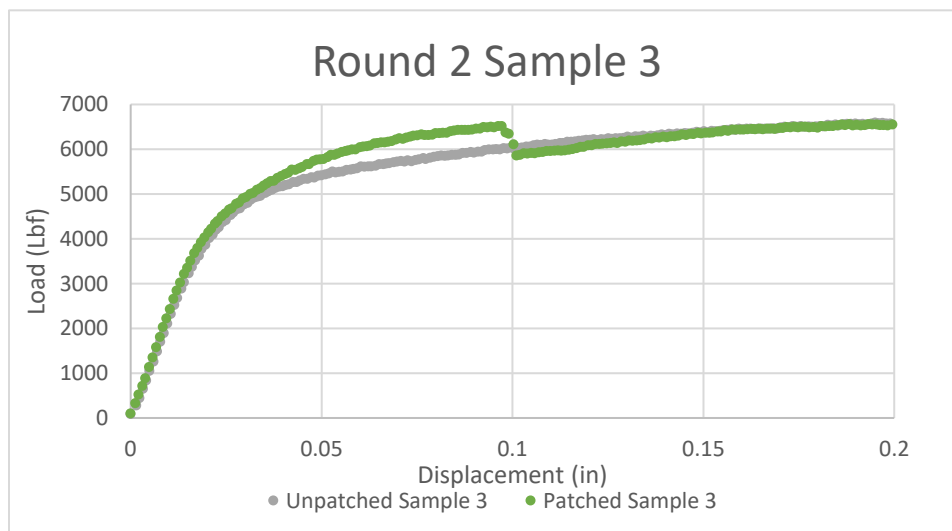
Rounds 2, 3 and 4 of tests are shown in Graph 8.4-Graph 8.7 in every round it can be seen that the patched samples show an increase in load bearing ability as the sample yields. There is a sudden decrease in the load of the patched samples, while testing in the lab an audible crack was heard at the same time as the load decrease. After the load drops the curve closely returns to that of a sample that was unpatched, this indicates that a distinct drop in load occurs when the patch fails, and its effects are no longer seen.



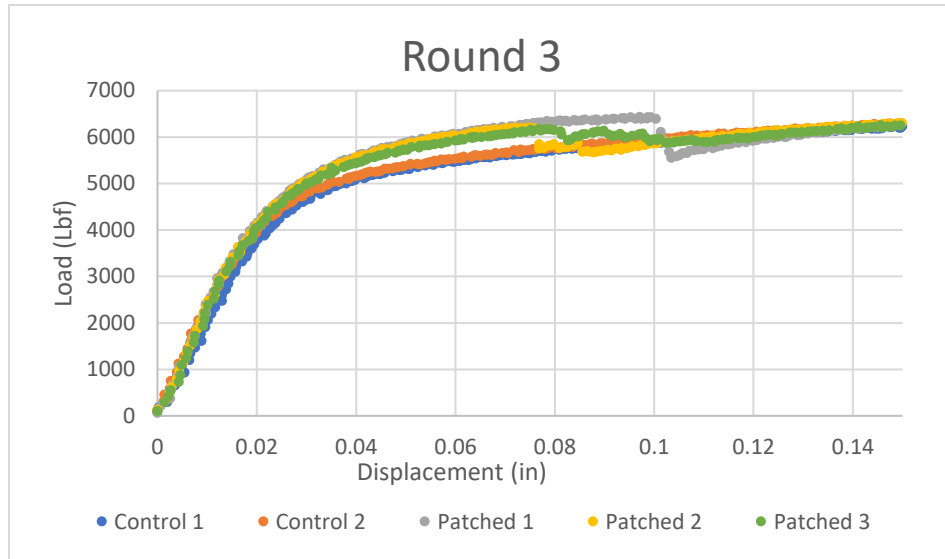
Graph 8.4 Round 2 sample 1 Patched VS. Unpatched



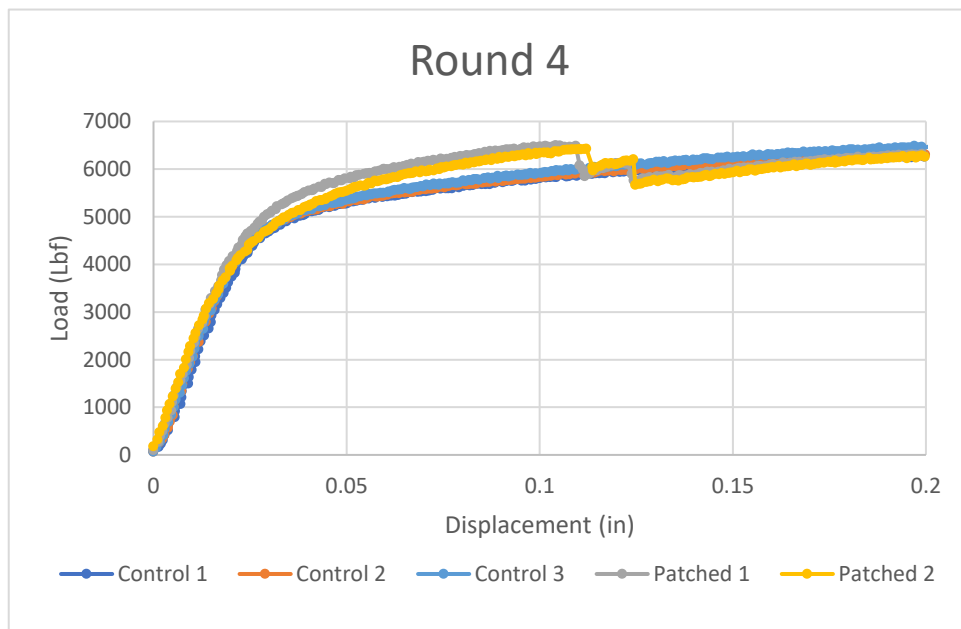
Graph 8.5 Round 2 sample 2 Patched VS. Unpatched



Graph 8.6 Round 2 sample 3 Patched VS. Unpatched



Graph 8.8 Round 3 Patched VS. Unpatched



Graph 8.7 Round 4 Patched VS. Unpatched

CHAPTER 9

PATCH DURABILITY STUDY IN NEAR MARINE ENVIRONMENTS

After proving that the patch was effective in increasing the load bearing ability of the SS sample, it now becomes important to determine the durability of the patch in a harsh corrosive environment. A laboratory easy-to-control environmental chamber that could simulate desired environmental conditions and/or create corrosive conditions on test samples was designed and developed. A variety of samples including pristine, cracked without patch, and cracked with patch are placed in the chamber subject to different conditions and/or duration. Subsequent loading tests are performed to assess how the environmental conditions could possibly affect the samples, the patching, and/or if they can cause SCC to occur.

9.1 DESIGN AND PREPARATION OF AN ENVIRONMENTAL CHAMBER.

The design of this environmental chamber had a few key requirements that needed to be met: A) the temperature must be controlled and able to sustain 50° C, B) the system must be able to control the humidity at a level of $\pm 10\%$ up to 75%, C) the system must be able to operate continuously for weeks between shutdowns. When researching for examples of cost-effective ways to meet these requirements one design was found published by Fluoramics, inc.[29]. This design called for a plastic container, an internal mounting frame, silicone heating pad, and an ultrasonic fogger. This design was intended

to meet the ASTM B117 Standard, by having a controlled temperature of 100° F, a 5% salt solution, and a condensing fog environment.

Fluoramics plan calls for an ultrasonic mister to be placed into the heated chamber with the test samples. The corrosion-resistant ultrasonic mister that was used came with a warning from the manufacturer recommending that the water temperature not exceed 37° C. (100° F). To ensure that the mister remained in proper working conditions the design was changed to that shown in Figure 9.1. In this design a waterproof fan designed for high humidity enclosures would push air across the heating elements while pulling air from the mister area. This would keep the mister and fan cool while creating airflow to help keep the temperature even throughout. The parts to control the humidity were sourced from The House of Hydro, who specialize in humidity control of small and medium rooms, as well as a variety of specialized projects. Figure 9.2 shows an early attempt to prove that we had the ability to control temperature and humidity. This was constructed using a plastic storage container that is chemically resistant, Keenovo 300 mm by 300 mm flexible silicone heating pads, aluminum flexible 4 in duct, a 5-gallon food grade bucket, and 3D printed adapters that fit the ducts to the different surfaces made of PETG, a medium-high temperature rated plastic. A Taylor indoor/outdoor weather station was selected to measure the temperature and humidity inside the chamber for its ability to withstand harsh environments. Finally, a layer of insulation was added around the container to help retain the heat.

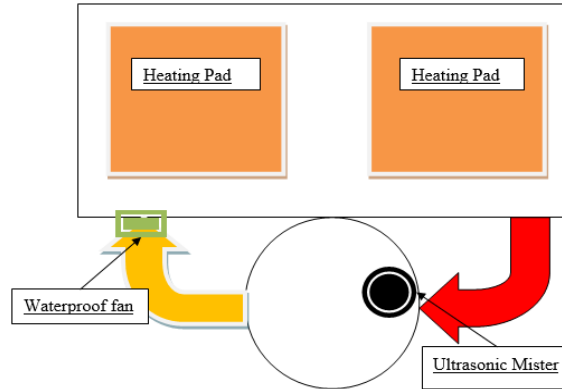


Figure 9.1 Design graphic for environmental chamber.

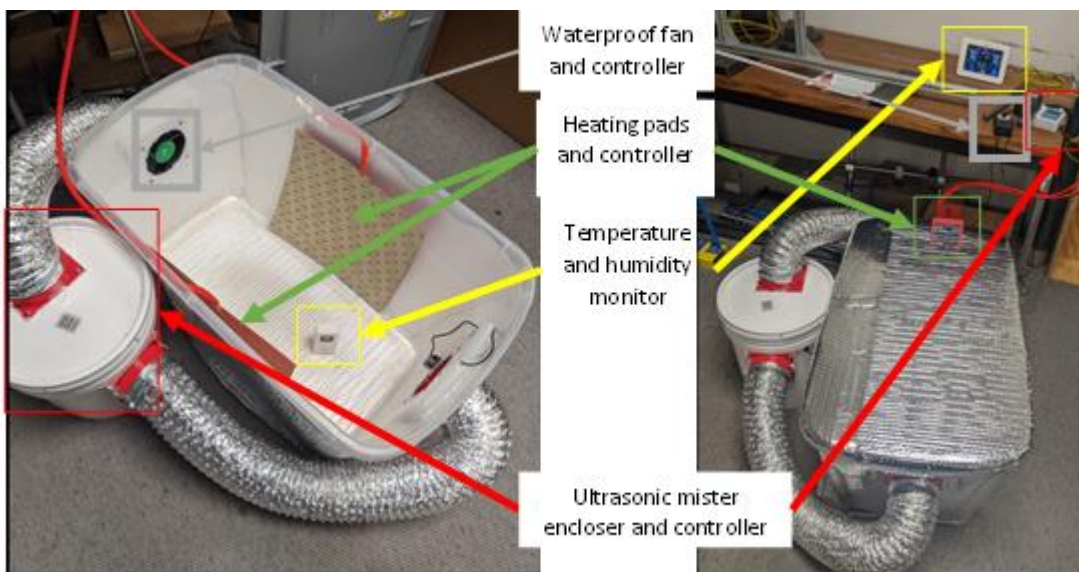


Figure 9.2 Proof of concept construction of environmental chamber

This system was run with no corrosive agent for a period of 48 hours to verify that the system could reach a stable temperature and humidity. After the 48-hour period, the temperature was elevated and held steadily, at 30° C, and the humidity was stable at 75 %.

After concluding the 48-hour test of the primary systems it became clear that with refinement the system could meet our goals. There were 4 key refinements made, first, the insulation was increased to further reduce the amount of heat loss. Second a drain was added to allow any condensation that collects to drain back to the mister enclosure, this

drastically decreased the water consumption. Third, a diffuser was added to redirect the airflow through the chamber. Finally, an internal structure was created to support test samples, as well as act as a heat sink for the heating pads. This heat sink effect increases the surface area used for convection. Figure 9.3 shows the chamber with these refinements implemented at the start of another proof test. This test was run for 24 hours with the corrosive agent. This corrosive agent is simulated seawater made following ASTM D1141-98. During this test the temperature was monitored using the weather station, as well as 4 other k-type thermocouple temperature probes, this was done to verify the temperature distribution throughout the chamber.

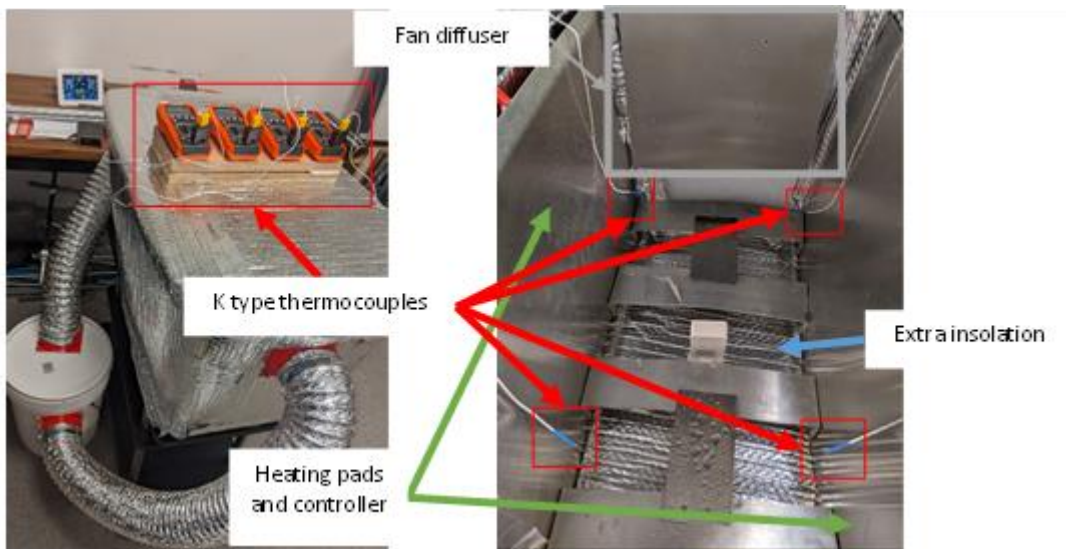


Figure 9.3 Environmental chamber with refinements implemented and labeled, NOT shown is drain.

9.2 ACCELERATED ENVIRONMENTAL EXPOSURE TESTS

In this study, we looked at how extended time exposed to the corrosive environment discussed previously would affect the strength of a stainless-steel sample, as well as its effects on the previously decided upon patching design. The test plan was to

have multiple groups of samples both patched and unpatched that would be exposed for an increasing amount of time. Table 9.1 provides the grouping of samples, and the exposure time. During this exposure, the environmental conditions were monitored once daily, just before the samples were removed to apply the artificial seawater solution. The samples were arranged so that the surface to be corroded was facing the center of the chamber, and the other side was protected to prevent the saltwater solution from reaching the surface. Figure 7.4 shows the arrangement of the samples in the chamber. Every day corrosive agent was applied, and the samples were rotated around the chamber. The rotation ensures that there is an even amount time spent in any one portion of the chamber to account for any discontinuous conditions.

Table 9.1 Preliminary accelerated corrosive environment exposure test groups.

Group #	Exposure time	# of unpatched samples	# of patched samples
0	0	3	3
1	14 days	3	3
2	30 days	3	3

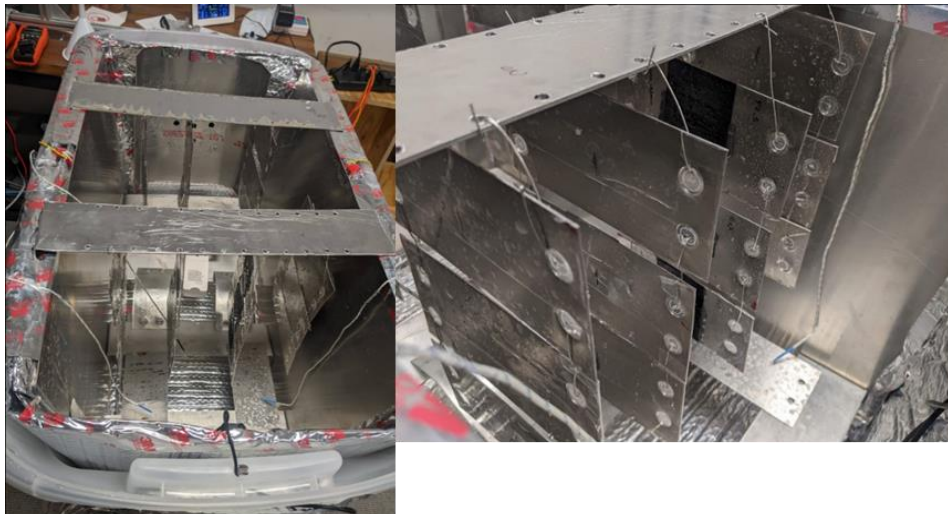


Figure 9.4 Sample arrangement inside the environmental chamber.

Figure 9.5 shows selected samples from each of the groups in the Preliminary round of environmental testing. Each sample was tested using the testing method developed previously. In this case, a layer of clear tape was applied to each sample to prevent corrosion from occurring on the back side and gripping surfaces. In Graph 9.1 it can be seen that the failure point for Group 1 is significantly reduced from that of group 0, it was decided that two changes be made: A) a different epoxy should be explored, and B) the tape should be replaced by a method that would prevent corrosion more evenly. The second epoxy that was explored and ultimately used throughout the remainder of testing was the HighHeat J-B WELD. The HighHeat epoxy, is rated up to 550° F, cures in 24 hours at room temperature, however the curing time can be decreased down to 1 hour, by increasing the temperature to 250° F [30].

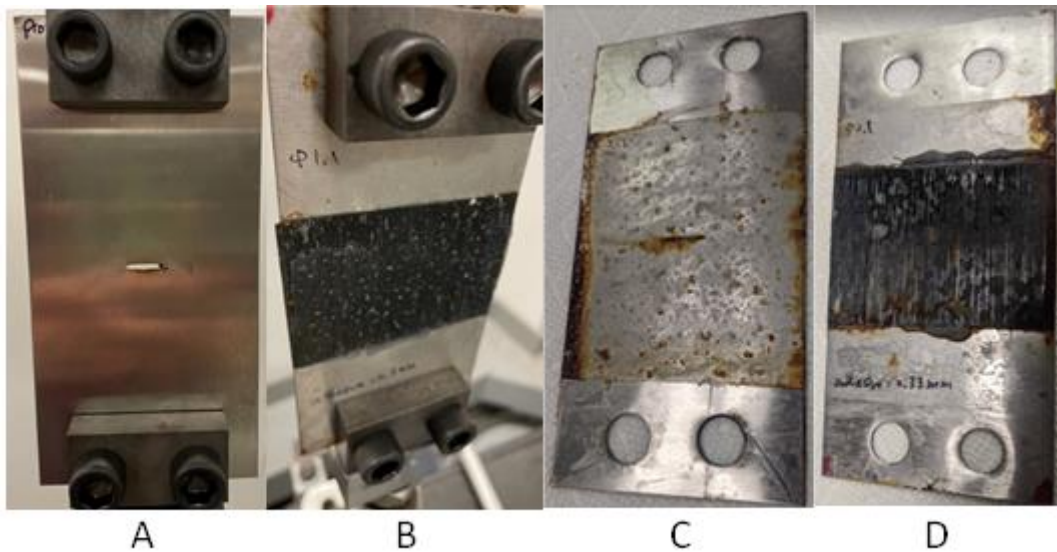
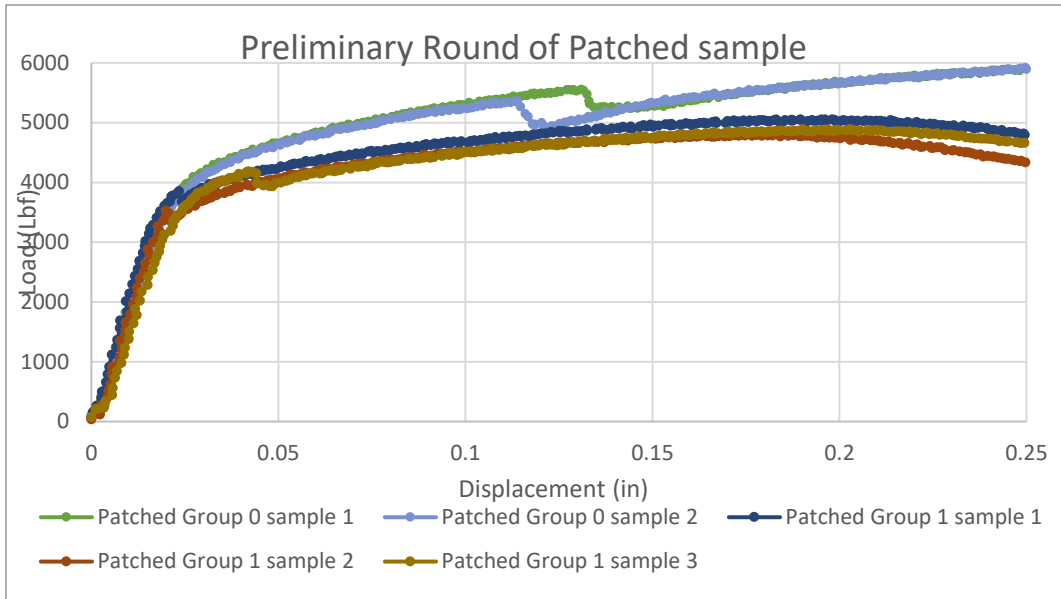


Figure 9.5 Example test samples: A) Control no exposure B) 15 days exposed patched C) 30 days exposed unpatched D) 30 days exposed patched.



Graph 9.1 Preliminary Patches sample comparison between Groups 0 and 1.

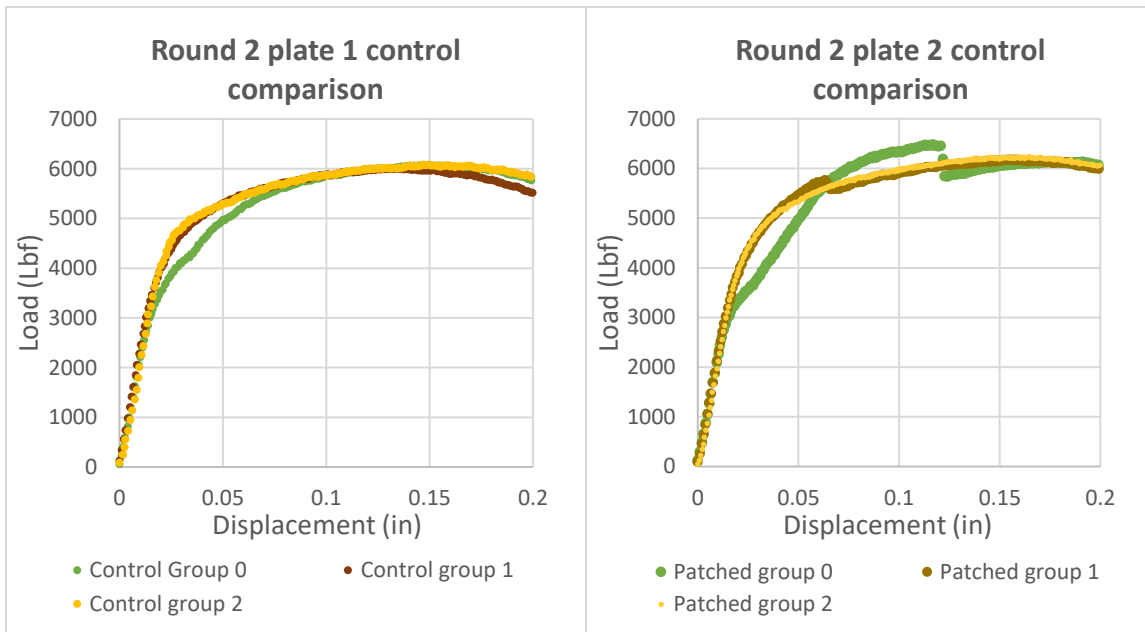
9.3 RESULTS OF THE EFFECTS OF EXPOSURE ON PATCH STRENGTH

To prove the effectiveness of our environmental chamber and its ability to degrade the strength of the SS substrate, the unpatched samples from each testing groups were compared for the max load. A total of four rounds of testing were performed with a variety of different environmental conditions. Table 9.2 lists the conditions during the duration of each round. The air temperature was maintained with an accuracy of $\pm 2^{\circ}\text{C}$, and the humidity $\pm 10\%$.

Table 9.2 Table 7.2: Exposure testing environmental conditions by round.

Test Round #	Corrosion Prevention Method	Air Temperature	Relative Humidity
Preliminary	Tape	40	80
2	High Temp Paint	40	80
3	High Temp Paint	40	50
4	High Temp Paint	50	40

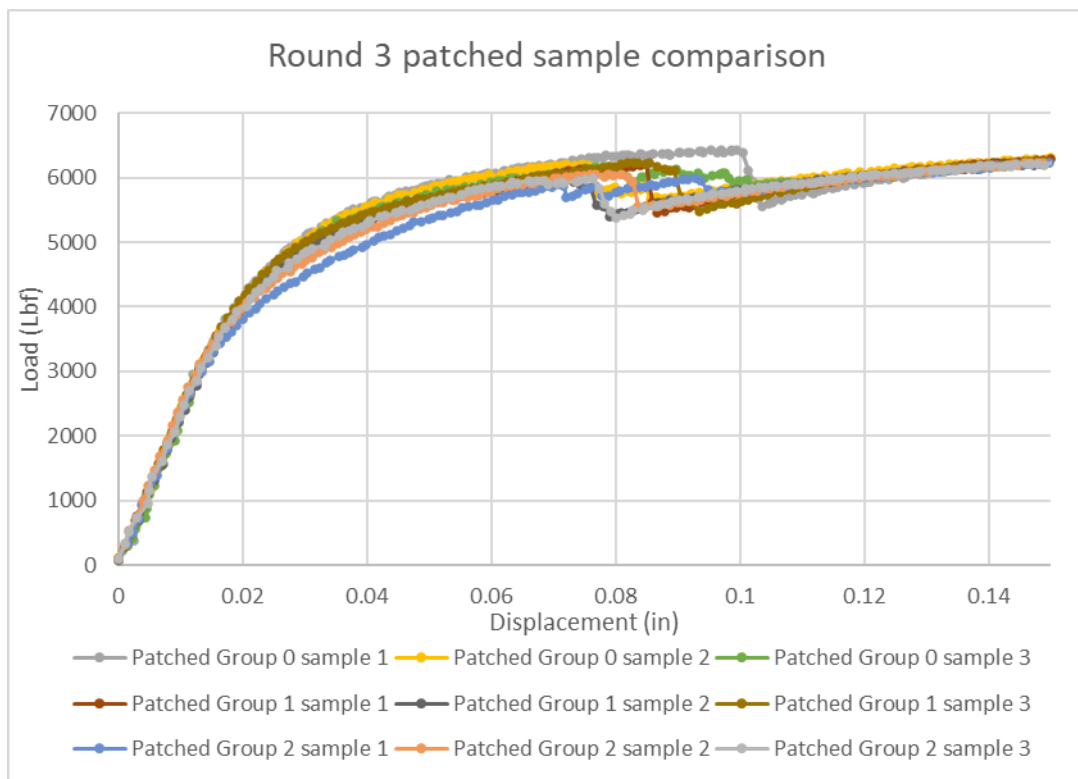
With the success of the preliminary studies, we conducted another round of loading tests on the exposed samples, denoted as Round 2. In this round, the peak load of each test was averaged within its exposure group, this average was 6285 lbf for group 0, it decreased to 6275 for group 1 and to 6268 in group 2. This indicates that the chamber at 40° C and 80% humidity had a small effect over the sample strength. Graph 9.2 shows the comparison of the control plates, and Graph 9.3 shows the comparison of the patched samples. While there was a small decrease in the average max strength of the samples, the patches effect was strongly impacted, with group 2 seeing no clear debonding.



Graph 9.2 Comparison of Round 2 plate one groups

Graph 9.3 Comparison of Round 2 plate two groups

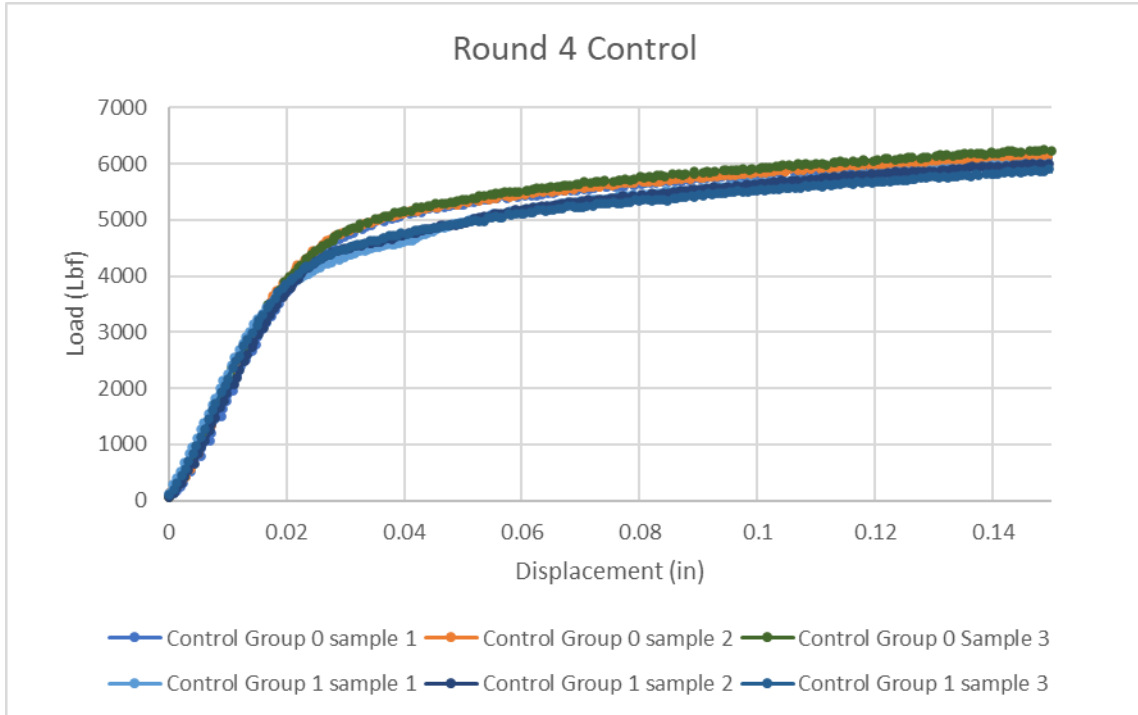
In Round 3 tests, the average peak load for the control samples in group 0 was 6545 lbf, 6542 lbf for group 1 and 6598 lbf in group 2. This indicates that the chamber at 40° C and 50% humidity had no significant effect over the sample strength. Graph 9.4 Round 3 patched sample comparison shows the comparison of the patched samples. There was a small decrease in the patches effect, however the reduction is still in the plastic deformation region.



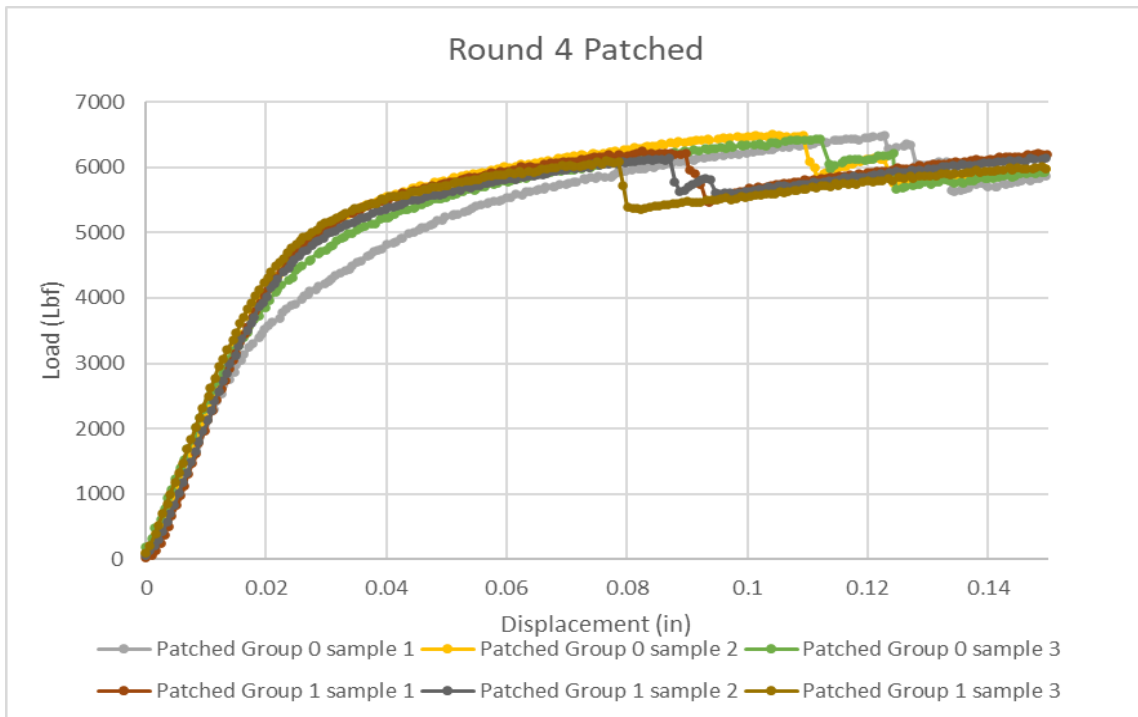
Graph 9.4 Round 3 patched sample comparison

In the last round (Round 4) only groups 0 and 1 were tested, these groups had an average control peak of 6307 lbf and 6235 lbf respectively. A 1.15% decrease, indicating that there was a small amount of damage caused by the environment, (50° C and 40% humidity). The average peak load before patch debonding for the patched samples

dropped to 6473 lbf down to 6149 lbf, a 5% decrease. In group 0 all 3 deboned after 0.110 inches, however in group 1 all patches had failed at .090 inches.



Graph 9.6 Round 4 Control Samples



Graph 9.5 Round 4 Patched Samples

CHAPTER 10

PART II CONCLUSION

Given the results from the test cases presented, we conclude that the designed composite patch does not adversely affect the host structure mechanical properties within the linear range when bonded and shows being effective in increasing the load bearing capability of the invested test samples by an average of 460 lbf before any debonding is seen. The durability of this patch under simulated and accelerated environmental conditions has been evaluated. The investigation in this work shows that the exposure to the laboratory accelerated corrosive, near marine environment has a significant effect on the bond strength as exposure time increased the effective bond strength is decreased. It is the suggestion of the author that this be further studied, with a specific focus on the recreation of the environments that are created within the dry cast storage facilities cooling passages.

REFERENCES

- [1] E. Compton, "Nondestructive Material Characterization Using A Fully Non-Contact Ultrasonic Lamb Wave System For Thin Metals, Nuclear Cladding, And Composite Materials" Masters Thesis, Coll. of Eng. and Computing, Univ. of South Carolina, Columbia, 2022.
- [2] Z. Ma, "Lamb Wave Nondestructive Evaluation and Imaging on Plate-Like Structures" Ph.D. dissertation, Coll. of Eng. and Computing, Univ. of South Carolina, Columbia, 2020.
- [3] Z. Ma and L. Yu, "Lamb wave defect detection and evaluation using a fully non-contact laser system", Proc. SPIE 10972, Health Monitoring of Structural and Biological Systems XIII, 1097221, 1 April 2019.
- [4] Z. Tian, S. Howden, Z. Ma, W. Xiao, and L. Yu, "Pulsed laser-scanning laser doppler vibrometer (PL-SLDV) phased arrays for damage detection in aluminum plates," Mechanical Systems and Signal Processing, vol. 121, pp. 158-170, 2019.
- [5] Y. Hayashi, S. Ogawa, H. Cho, and M. Takemoto, "Non-contact estimation of thickness and elastic properties of metallic foils by laser-generated Lamb waves," Ndt & E International, vol. 32, no. 1, pp. 21-27, 1999.
- [6] University of South Carolina. "Basic Laser Safety," 1 July 2011. [Online] Available: https://sc.edu/about/offices_and_divisions/ehs/documents/lasermanual.pdf
- [7] S. E. Ferry, B. P. Black, S. Teyseyre, and R. G. Ballinger, "The Effect of Weld Residual Stress on Life of Used Nuclear Fuel Dry Storage Canisters," presented at the 16th International Conference on Environmental Degradation of Materials in Nuclear Power System-Water Reactors, 2013.
- [8] C. R. Bryan and D. G. Enos, "Understanding the Environment on the Surface of Spent Nuclear Fuel Interim Storage Containers," Sandia National Laboratories, Albuquerque, NM, USA2014.
- [9] A. Kosaki, "Evaluation Method of Corrosion Lifetime of Conventional Stainless-Steel Canister under Oceanic Air Environment," Nuclear Engineering and Design, vol. 238, pp. 1233-1240, 2008.
- [10] S. Ghosh and V. Kain, "Effect of Surface Machining and Cold Working on the Ambient Temperature Chloride Stress Corrosion Cracking Susceptibility of AISI 304L Stainless Steel," Materials Science & Engineering A, vol. 527, pp. 679-683, 2010.
- [11] D. Deng, H. Murakawa, and W. Liang, "Numerical and Experimental Investigations on Welding Residual Stress in Multi-Pass Butt-Welded Austenitic Stainless Steel Pipe," Computational Materials Science, vol. 42, pp. 234-244, 2008.
- [12] S. Choi, H. Cho, and C. J. Lissenden, "Nondestructive Inspection of Spent Nuclear Fuel Storage Canisters Using Shear Horizontal Guided Waves," Nuclear Engineering and Technology, vol. 50, pp. 890-898, 2018.

- [13] B. Lin, D. Dunn, and R. Meyer, "Evaluating the Effectiveness of Nondestructive Examinations for Spent Fuel Storage Canisters," AIP Conference Proceedings, vol. 2102, 2019.
- [14] A. K. Bakare, A. A. Shaikh, and S. S. Kale, "Comparison of SCC behavior of Crack in thin Aluminium Structure With and Without Single Sided Composite Patch Repair," Engineering Failure Analysis, vol. 118, 2020.
- [15] Z. Marioli-Riga and E. E. Gdoutos, "Composite Patch Repair Methodology for Damaged Aircraft Structural Components," presented at the 2004 SEM Annual Conference, 2004.
- [16] J. G. Teng, T. Yu, and D. Fernando, "Strengthening of Steel Structures with Fiber-reinforced Polymer Composites," Journal of Constructional Steel Research, vol. 78, pp. 131-143, 2012.
- [17] L. V. D. Eide, L. Zhao, and F. Seible, "Use of FRP Composites in Civil Structural Applications," Construction and Building Materials, vol. 17, pp. 389 - 403, 2003.
- [18] E. P. Douglas, H. R. H. III, J. Nino, A. Stewart, and J. Tatar, "Highly Accelerated Lifetime for Externally Applied Bond Critical Fiber-reinforced Polymer (FRP) Infrastructure Materials," Department of Materials Science & Engineering, University of Florida 2014.
- [19] C. L. Soles and A. F. Yee, "A Discussion of the Molecular Mechanisms of Moisture Transport in Epoxy Resins," Journal of Polymer Science: Part B: Polymer Physics, vol. 38, pp. 792-802, 2000.
- [20] P. Colombi, G. Fava, and L. Sonzogni, "Effect of Initial Damage Level and Patch Configuration on The Fatigue Behaviour of Reinforced Steel Plates," Fatigue & Fracture of Engineering Materials & Structures, vol. 38, pp. 368 - 378, 2015.
- [21] D. Schnerch, M. Dawood, S. Rizkalla, and E. Sumner, "Proposed Design Guidelines for Strengthening of Steel Bridges with FRP Materials," Construction and Building Materials, vol. 21, pp. 1001-1010, 2007.
- [22] M. Kamruzzaman, M. Z. Jumaat, N. H. R. Sulong, and A. B. M. S. Islam, "A Review on Strengthening Steel Beams Using FRP under Fatigue," The Scientific World Journal, 2014.
- [23] A. C. Okafor and H. Bhogapurapu, "Design and Analysis of Adhesively Bonded Thick Composite Patch Repair of Corrosion Grind-out and Cracks on 2024 T3 Clad Aluminum Aging Aircraft Structures," Composite Structures, vol. 76, pp. 138-150, 2006.
- [24] Y. Ayaz, Ş. Çitil, and M. F. Şahan, "Repair of Small Damages in Steel Pipes with Composite Patches," Materials Science & Engineering Technology, vol. 47, pp. 503 - 511, 2016.
- [25] C. Wu, X.-L. Zhao, R. Al-Mahaidi, M. R. Emdad, and W. Duan, "Fatigue Tests of Cracked Steel Plates Strengthened with UHM CFRP Plates," Advances in Structural Engineering, vol. 15, 2012.
- [26] Huntsman ARALDITE® 2013-1 Resin "SAFETY DATA SHEET" version 1.4, URL: <https://docs.rs-online.com/9564/0900766b816d58fa.pdf>, 2021
- [27] A. A. E. Damatty and M. Abushagur, "Testing and Modeling of Shear and Peel behavior for Bonded Steel/FRP Connections," Thin-walled Structure, vol. 41, pp. 987-1003, 2003.

- [28] “Dremel 76-piece Variable speed corded 1.8-amp multipurpose rotary tool ...” (2022). *Lowes.com*, <<https://www.lowes.com/pd/Dremel-76-Piece-Variable-Speed-Corded-1-8-Amp-Multipurpose-Rotary-Tool-with-Hard-Case/1001858818>> (Aug. 15, 2021).
- [29] “How to make an inexpensive salt-fog chamber.” (2017). *Fluoramics*, <<https://www.fluoramics.com/how-to-construct-an-inexpensive-salt-fog-chamber/20/>> (Nov. 22, 2022).
- [30] JB weld High Heat Epoxy “Safety data sheet,” URL: https://dynamix-cdn.s3.amazonaws.com/jbweldcom/jbweldcom_134187590.pdf, 2019